arXiv:astro-ph/0611414v1 14 Nov 2006

Exploring Broadband GRB Behavior During γ-ray Emission

Yost, S. A.[1], Swan, H. F.[1], Rykoff, E. S.[1], Aharonian, F.[2], Akerlof, C. W.[1], Alday, A.[3], Ashley, M. C. B.[4], Barthelmy, S.[5], Burrows, D.[6], Depoy, D. L.[7], Dufour, R. J.[8], Eastman, J. D.[7], Forgey, R. D.[9], Gehrels, N.[5], Göğüş, E.[10], Güver, T.[11], Halpern, J. P.[12], Hardin, L. C.[9], Horns, D.[2], Kızıloğlu, Ü.[13], Krimm, H. A.[5,14], Lepine, S.[15], Liang, E. P.[8], Marshall, J. L.[7], McKay, T. A.[1], Mineo, T.[16], Mirabal, N.[12], Özel, M.[17], Phillips, A.[4], Prieto, J. L.[7], Quimby, R. M.[18], Romano, P. [19], Rowell, G.[2], Rujopakarn, W.[1], Schaefer, B. E.[20], Silverman, J. M.[21], Siverd, R.[7], Skinner, M.[5], Smith, D. A.[1,22], Smith, I. A.[8], Tonnesen, S.[12], Troja, E.[16], Vestrand, W. T.[21], Wheeler, J. C.[18], Wren, J.[23], Yuan, F.[1], Zhang, B.[24]

[1]University of Michigan, 2477 Randall Laboratory, 450 Church St., Ann Arbor, MI, 48104, sayost@umich.edu, hswan@umich.edu, erykoff@umich.edu, akerlof@umich.edu, tamckay@umich.edu, wiphu@umich.edu, donaldas@umich.edu, yuanfang@umich.edu

[2]Max-Planck-Institut für Kernphysik, Saupfercheckweg 1, 69117 Heidelberg, Germany, Felix.Aharonian@mpi-hd.mpg.de, horns@mpi-hd.mpg.de, rowell@mpi-hd.mpg.de

[3]Boeing LTS, AMOS Observatory, Kihei, Maui, Hawaii, andrew.alday-iii@boeing.com, mark.a.skinner@boeing.com

[4]School of Physics, Department of Astrophysics and Optics, University of New South Wales, Sydney, NSW 2052, Australia, mcba@phys.unsw.edu.au, a.phillips@unsw.edu.au

[5]NASA/Goddard Space Flight Center, Greenbelt, MD 20771, scott@lheamail.gsfc.nasa.gov, gehrels@gsfc.nasa.gov, krimm@milkyway.gsfc.nasa.gov

[6]Department of Astronomy, Penn State, 525 Davey Lab, University Park, PA 16802, dburrows@astro.psu.edu

[7]Department of Astronomy, Ohio State University, 140 West 18th Avenue, Columbus, OH, 43210, depoy@astronomy.ohio-state.edu, jdeast@astronomy.ohio-state.edu, marshall@astronomy.ohio-state.edu, prieto@astronomy.ohio-state.edu, siverd@astronomy.ohio-state.edu

[8]Rice University, Department of Physics and Astronomy 6100 South Main, MS 108, Houston, TX, 77251-1892, rjd@rice.edu, liang@spacibm.rice.edu, ian@spacibm.rice.edu

[9]Hardin Optical Company, P.O. Box 219, Bandon, OR 97411, bob@hardinoptical.com, larry@hardinoptical.com

[10]Sabancı University, Orhanlı-Tuzla 34956 Istanbul, Turkey, ersing@sabanciuniv.edu

[11]Istanbul University Science Faculty, Department of Astronomy and Space Sciences, 34119, University-Istanbul, Turkey, tolga@istanbul.edu.tr

[12]Columbia University, Columbia Astrophysics Lab, 550 W. 120th St. Mail Code 5230, New York, NY 10027-6601, jules@astro.columbia.edu, mirabal@astro.columbia.edu, stonnes@astro.columbia.edu

[13]Middle East Technical University, 06531 Ankara, Turkey, umk@astroa.physics.metu.edu.tr

[14]Universities Space Research Association, 10211 Wincopin Circle, Suite 500, Columbia, MD 21044-3432, krimm@milkyway.gsfc.nasa.gov

[15]Department of Astrophysics, Division of Physical Sciences, American Museum of Natural History, Central Park West at 79th Street, New York, NY 10024 lepine@amnh.org

[16]INAF, Via U. La Malfa 153, 90146 Palermo, Italy teresa.mineo@ifc.inaf.it, nora@ifc.inaf.it

[17]Çanakkale Onsekiz Mart Üniversitesi, Terzioğlu 17020, Çanakkale, Turkey, m.e.ozel@comu.edu.tr

[18]Department of Astronomy, University of Texas, Austin, TX 78712, quimby@astro.as.utexas.edu, wheel@astro.as.utexas.edu

[19]Osservatorio Astronomico di Brera, Via Bianchi 46, 23807 Merate LC, Italy, pa-

ABSTRACT

The robotic ROTSE-III telescope network detected prompt optical emission contemporaneous with the γ-ray emission of *Swift* events GRB 051109A and GRB 051111. Both datasets have continuous coverage at high signal-to-noise levels from the prompt phase onwards, thus the early observations are readily compared to the *Swift* XRT and BAT high energy detections. In both cases, the optical afterglow is established, declining steadily during the prompt emission. For GRB 051111, there is evidence of an excess optical component during the prompt emission. The component is consistent with the flux spectrally extrapolated from the γ-rays, using the γ-ray spectral index. A compilation of spectral information from previous prompt detections shows that such a component is unusual. The existence of two prompt optical components — one connected to the high-energy emission, the other to separate afterglow flux, as indicated in GRB 051111 — is not compatible with a simple "external-external" shock model for the GRB and its afterglow.

Subject headings: gamma rays:bursts

1. Introduction

Gamma-ray burst (GRB) early emission observations have become routine since the launch of the *Swift* satellite (Gehrels et al. 2004). This satellite has provided prompt triggers to events since early 2005, whereby "prompt" designates "during γ-ray emission". With the combination of such triggers and the increasing number of automated rapid-response

trizia.romano@brera.inaf.it

[20]Department of Physics and Astronomy, Louisiana State University, Baton Rouge, LA 70803, schaefer@lsu.edu

[21]Astronomy Department , University of California at Berkeley, Berkeley, CA 94720-3411, JSilverman@astro.berkeley.edu

[22]Guilford College, 5800 West Friendly Ave., Greensboro, NC 27410, dsmith4@guilford.edu

[23]Los Alamos National Laboratory, NIS-2 MS D436, Los Alamos, NM 87545, vestrand@lanl.gov, jwren@nis.lanl.gov

[24]Physics Department, University of Nevada, Las Vegas, NV 89154, bzhang@physics.unlv.edu

telescopes, the GRB field now has several examples of optical lightcurves that begin during, or within seconds after, the γ-ray emission.

Broadband prompt emission is one of the least-understood aspects of GRB phenomena. The first prompt optical detection, GRB 990123 (Akerlof et al. 1999), exhibited an optical flare that was interpreted as the signature of a reverse shock passing through the relativistic ejecta (however, for another interpretation, see Liang et al. 1999). Reverse shock emission was expected to be common (Sari & Piran 1999), so it has come as a surprise that nearly all rapidly-detected GRB afterglows show scant evidence of it. There are alternatives to the standard "internal shocks" formulation for prompt emission. Such models include, e.g., external shocks (Meszaros & Rees 1993) or magnetic reconnection (Meszaros et al. 1994; Thompson 1994; Usov 1994) as the mechanism to release energy as γ-rays. The nature of GRB prompt emission is best investigated in conjunction with prompt observations at lower frequencies, with ongoing measurements at the same frequency to connect to the longer-lasting, and better understood, afterglow.

The *Swift* XRT's early X-ray observations have revealed a nearly standard morphology seen in most bursts' X-ray afterglow (Nousek et al. 2006; O'Brien et al. 2006). The typical early X-ray afterglow includes two surprises: a stage of relatively slow decay preceding the faster decline, known from pre-*Swift* observations, hours to days post-burst, and flaring well after the cessation of γ-ray emission. To connect this interesting early behavior to the later afterglow evolution, it is essential to compare such high-energy emission to lower-energy evolution. Such comparisons elucidate which features also occur at low energies, indicating a process affecting the entire early afterglow rather than a separate high-energy component (see GRB 050801, Rykoff et al. 2006).

There is a small but growing sample of events for which it is possible to compare the very early optical lightcurve with X-ray emission (or in the case of prompt optical detections, the GRB emission itself). To date no consistent connection between prompt optical observations and the contemporaneous γ-rays has emerged (e.g., see the discussion in Rykoff et al. 2005b). We present here two new cases of contemporaneous optical and high-energy observations. For GRB 051109A, the initial optical detection is prompt with respect to the γ-rays, and is followed by significant overlap with X-ray observations. GRB 051111 does not have early X-ray observations, but the optical lightcurve has significant temporal overlap (several detections) with the *Swift* BAT γ-ray detections.

The structure of the paper is as follows. The events and our observations are described in § 2. § 3 gives technical details for the data reduction, and §§ 4,4.1, and 4.3 detail the optical and high-energy transformations to spectral flux densities. §§ 4.2 and 4.4 indicate the key features of the optical and high-energy lightcurves, respectively. We discuss the lightcurves

in the context of the fireball model of afterglows. § 5 summarizes important spectral and temporal predictions of this model. The subsequent sections discuss the lightcurves and broadband comparisons. § 6 compares optical and X-ray in GRB 051109A. It is divided into several subsections: § 6.1 examines the relative complexity of the X-ray during the first hour, as compared to the steadily declining optical, § 6.2 discusses the data near 0.5 day, suggestive of achromatic steepening, while § 6.3 looks at explanations and § 6.4 notes the similarity of the GRB 051111 optical lightcurve break near 1 ksec. § 7 analyzes the prompt optical emission of GRB 051111, which includes a flux excess while high-energy emission is detected. This excess is compared to other prompt cases. § 8 summarizes the conclusions.

We use α to indicate temporal decay indices, and β for spectral indices, with flux density $f_\nu \propto t^\alpha \nu^\beta$. To designate a spectral region, subscripts "OPT", "X", and "γ" indicate an index for the optical, X-ray, and γ-ray bands respectively. A spectral index spanning two regions is indicated with both, e.g., β_{OPT-X} for the spectral index interpolating between the optical and X-ray frequencies.

In the following, X-ray fluxes are measured in the band from 0.2–10 keV, and γ-ray fluxes correspond to 15–150 keV (in the observed frame). The spectral shapes of higher frequency bands are reported as photon indices, Γ ($dn/d\nu \propto \nu^\Gamma$). Note that the spectral index β is related to the photon index Γ, by $\beta = 1 - \Gamma$.

2. Observations

The optical observations presented were taken by three observatories. The instruments are described, followed by a description of the instruments' responses to the events, and the XRT response to GRB 051109A.

The ROTSE-III array is a worldwide network of 0.45 m robotic, automated telescopes, built for fast ($\sim$ 6 s) responses to GRB triggers from satellites such as HETE-2 and *Swift*. They have a wide ($1.^\circ85 \times 1.^\circ85$) field of view (FOV) imaged onto Marconi 2048×2048 back-illuminated thinned CCDs, and operate without filters, with sensitivity from approximately 400 to 900 nm. ROTSE-IIIb is located at McDonald Observatory in Texas. The ROTSE-III systems are described in detail in Akerlof et al. (2003).

The MDM Observatory is located at Kitt Peak, Arizona. It includes the 1.3m and the 2.4m Hiltner telescope. The 2.4m has three CCDs, with FOVs from 3.3 to 9.6 arcmin, which were used for the GRB 051109A observations. RETROCAM is the Retractable Optical Camera for Monitoring, an Apogee ALTA E55 (1152×770 pixels, with a scale of $0\farcs26$ per pixel). Wilbur is a LORAL front side-illuminated CCD (2048×2048 pixels, with a scale of

0.″17 per pixel). Echelle is an SITe thinned, back side-illuminated CCD (2048 × 2048 pixels, with a scale of 0.″28 per pixel). These CCDs operate with standard filters. The 1.3m has an SITe backside illuminated CCD (17′FOV, with 0.″508 per pixel), with a Harris R filter used for the late observation of GRB 051111. Further details for all instruments are available at the MDM website[1]

The RUCCD instrument is installed on the 3.67 m Advanced Electro-Optical System (AEOS) telescope at the Air Force Maui Optical and Supercomputing (AMOS) site, located at 10,033 ft in Haleakala, Hawaii. The camera is a 2048 × 2048 front-illuminated CCD, covering a 45″ FOV. The instrument incorporates an extensive set of optics options (polarizers, gratings, and filters), which includes standard V, R and I filters. The RUCCD system is described in detail in Smith et al. (2005).

2.1. GRB 051109A

On 2005 November 9, *Swift* detected GRB 051109A (*Swift* trigger 163136) at 01:12:20 UT. The position was distributed as a Gamma-ray burst Coordinates Network (GCN) notice at 01:12:49 UT, with a 3′ radius error box, 29 s after the start of the burst (Tagliaferri et al. 2005). The burst had a duration of 36 ± 2 s (90% duration, 15–350 keV), with a fluence of $2.1 \times 10^{-6}\,\mathrm{erg\,cm^{-2}}$ in the 15–150 keV band (Fenimore et al. 2005). Quimby et al. (2005) measured an absorption redshift of 2.346 for the event with the HET telescope, a few hours after the burst.

ROTSE-IIIb responded automatically to the GCN notice, with the first exposure starting at 01:12:52.7 UT, 32 s after the burst onset and before the cessation of γ-ray activity. The automated scheduler began a program of ten 5-s exposures, ten 20-s exposures, and 202 60-s exposures. Near real-time analysis of the ROTSE-III images detected a 15^{th} magnitude fading source at $\alpha = 22^h01^m15\overset{s}{.}3$, $\delta = +40°49'23\overset{''}{.}3$ (J2000.0) that was not visible on the Digitized Sky Survey[2] red plates. This was reported via the GCN Circular e-mail exploder within 9 minutes of the burst (Rykoff et al. 2005a).

Swift slewed immediately to the burst position, and the XRT began X-ray observations 120 sec after this trigger (Tagliaferri et al. 2005). An uncatalogued X-ray source was detected at $\alpha = 21^h01^m15\overset{s}{.}24$, $\delta = +40°49'23\overset{''}{.}2$, (J2000.0) with an estimated uncertainty of 3.5″ (90% confidence level), 0.7″ from the ROTSE coordinates. This position takes into account

[1] `http://mdm.kpno.noao.edu/`

[2] `http://archive.stsci.edu/cgi-bin/dss_form`

the correction for the misalignment between the telescope and the satellite optical axis (Moretti et al. 2006). Due to orbital pointing constraints, no XRT observations were made from $t \approx 200$–3000 sec, following which the field was visited continually for 16 days, for a total of ∼283 ksec in 18 observations.

The MDM Observatory began r-band observations 38 minutes after the burst, following the initial ROTSE GCN report. 23 exposures were taken of the GRB field, spanning a total of 2.5 hours. Over the next 12 days there were 4 further followup observations.

MDM reobserved the afterglow of GRB 051109A on 2006 June 29.456 UT (mid-exposure), approximately 20 Msec after the event. The observations consisted of four 600s R-band exposures acquired under superb (0″.8) seeing conditions. At the location of the afterglow, we detect a faint, extended object that we interpret to be the host galaxy of this event.

2.2. GRB 051111

On 2005 November 11, *Swift* detected GRB 051111 (*Swift* trigger 163438) at 05:59:41 UT. The position was distributed as a Gamma-ray burst Coordinates Network (GCN) notice at 06:00:02 UT, with a 3′ radius error box, 20.5 s after the start of the burst. The Moon's pointing constraint prevented *Swift*'s narrow-field instruments from being brought to bear on the GRB position immediately, and there are no early X-ray data (Sakamoto et al. 2005b). The burst had a 90% duration of 47 ± 1 s (15–350 keV), but there is extended emission to >80 s, and the burst's fluence was $3.9 \times 10^{-6}\,\mathrm{erg\,cm^{-2}}$ (15–150 keV) (Krimm et al. 2005a). Hill et al. (2005) measured an absorption redshift of 1.55 for the event with the HIRES instrument at the Keck telescope, an hour after the burst.

ROTSE-IIIb responded automatically to the GCN notice in 6.4 s with the first exposure starting at 06:00:08.4 UT, 26.9 s after the burst onset and before the cessation of γ-ray activity. The automated scheduler began a program of 10 5-s exposures, 10 20-s exposures, and 272 60-s exposures. Near real-time analysis of the ROTSE-III images detected a 13^{th} magnitude fading source at $\alpha = 23^h12^m33\overset{s}{.}2$, $\delta = +18°22'29\overset{''}{.}1$ (J2000.0) that was not visible on the Digitized Sky Survey[2] red plates, which we reported via the GCN Circular e-mail exploder within 8.3 minutes of the burst (Rujopakarn et al. 2005).

The RUCCD instrument responded to the GCN notice, with its first observation at 06:31:27 UT, 32 minutes after the burst. A series of 30-s observations of the GRB and a standard star were performed until 07:08:03 UT, using the VRI filters, and initially reported in Smith & Swan (2005).

The MDM 1.3m telescope performed observations 1 day after the GRB event. 75 minutes of R-band exposures were obtained over a period of 2 hours.

3. Data Reductions

3.1. Optical Data Reductions

ROTSE-III images were reduced and processed using the RPHOT pipeline, with routines based upon DAOPHOT (Stetson 1987). Objects were identified via SExtractor (Bertin & Arnouts 1996) and calibrated astrometrically and photometrically with the USNOB1.0 catalog. The method is fully described in Quimby et al. (2006), for the case of a well-separated counterpart, such as GRB 051111. The final result is a set of PSF-fit photometric data.

The ROTSE-III instruments have $3''.25$ pixels, and in the case of GRB 051109A the optical transient (OT) is partially blended with a nearby ($8''$) 17th magnitude star at $\alpha = 22^h01^m14\overset{s}{.}60$, $\delta = +40°49'25\overset{''}{.}3$. It was therefore necessary to remove this contaminating source prior to measuring the flux of the OT, especially in images where the OT's flux has faded to or below a similar level. To accomplish this, we first constructed a deep reference image using ROTSE-III data obtained well after the OT had faded below our detection limits. We measured the position and brightness of the contaminating star on this frame. The star is then removed from a given image by subtracting the locally determined PSF scaled to the appropriate flux level at the star's position.

With the contaminating source removed, the GRB 051109A OT light curve was extracted as described in Quimby et al. (2006). The PSF-fit and larger aperture light curves flatten out after $\sim$1 ksec post-burst. However, the light curve resulting from the smallest aperture (1σ radius, $\approx 3.5''$), which does not significantly overlap the contaminating star, instead continues fading at the same rate. This demonstrates that residual light from the nearby star remains despite our efforts to remove it. As the behavior of the 1σ radius aperture should have little contamination from the neighboring star, and since its light curve agrees with the behavior of the MDM data obtained simultaneously (see below), we adopt these results as the best estimate of the GRB 051109A OT light curve. There are no significant quantitative differences between the 1σ radius and PSF-fit flux estimates in frames when the OT was brighter than 17th mag. The estimated additional flux error due to slight misplacements of these small apertures is negligible and is not included in the results.

We have no data on afterglow color information for either GRB 051109A or GRB 051111 at early times. Thus, no additional color corrections for R-band equivalence have been applied to the ROTSE-III unfiltered data, and the magnitudes quoted are then treated as

R-band and referred to as "C_R".

The MDM data were processed using standard IRAF/DAOPHOT procedures. Aperture photometry was performed in a 1.″5 radius aperture (average seeing was a $\sim$1.″4 FWHM) centered on the OT and nearby field stars. All GRB 051109A observations, except the final two, were performed with Sloan or Gunn r filters. With no r standards in the MDM field, the GRB 051109A r observations are converted to an R-equivalent value and presented in Table 1 as "r_R". This is accomplished using differential photometry with respect to two USNOB1.0 R standards in the field (at α, $\delta = 22^h01^m15\overset{s}{.}663$, $+40°48'19\overset{''}{.}01$ and $22^h01^m10\overset{s}{.}444$, $+40°49'50\overset{''}{.}16$). The single GRB 051111 R-band point was calibrated with 5 USNOB1.0 stars within 3′ of the OT.

The late (host) observation of GRB 051109A used the same aperture size as the early OT observations (1.″5). As the seeing was good (0.″9), and the galaxy appears compact, the aperture includes the total light contribution of the galaxy. The measurement corresponds to $R_{host} = 23.70 \pm 0.16$, but does not change within the uncertainties when using aperture sizes from 0.″8–2.″1. Assuming the scaling of star-formation rate (SFR) to UV continuum luminosity of Kennicutt (1998), the implied uncorrected SFR in the host galaxy is $\approx$ 18 $M_\odot$ yr^{-1}. This value indicates a moderate SFR, when compared to starburst galaxies, as in previous cases (e.g., Christensen et al. 2004). Using an astrometric solution derived from a set of suitable field stars also present in earlier images, we find that the afterglow position is offset from the center of this galaxy by less than 0.″11 ($\pm$0.″15).

The RUCCD data were reduced using IRAF procedures and processed for aperture photometry with the IRAF 2.12.2 `qphot` package. A standard star, BD+42 4211, from the Bright Northern BVRI Standards[3] was observed between the two sets of GRB observations (the first set from 2–2.5 ksec, and the second from 3–4 ksec post-trigger). Its observations were used to reference the VRI GRB observations to absolute photometry.

The final optical magnitudes from these instruments are listed in the tables. Table 1 gives the GRB 051109A results, and Table 2 the GRB 051111 results.

3.2. High-Energy Data Reductions

The GRB 051109A XRT data were first processed by the *Swift* Data Center at NASA/GSFC into Level 1 products (event lists). This includes the initial 2.5 sec image, and the following Windowed Timing (WT) and Photon Counting (PC) observations (until 3440 sec, and after

[3] `http://stupendous.cis.rit.edu/tass/refs/skiff_photom.html`

3440 sec, post-trigger respectively) The event lists were further processed with the XRTDAS (v1.7.1; in FTOOLS) to produce the final cleaned event lists. In particular, the `xrtpipeline` (v0.9.9) applied calibration and standard filtering and screening criteria. Temporal intervals during which the CCD temperature was higher than −47 °C were cut out, and hot and flickering pixels were removed. An on-board event threshold of ∼0.2 keV was also applied to the central pixel, to reduce most of the background due to either the bright Earth limb or the CCD dark current. The events selected for analysis had XRT grades 0–12 and 0–2 for PC and WT data, respectively (for the *Swift* XRT nomenclature, see Burrows et al. 2005).

The GRB 051109A WT data were extracted in a rectangular region 40 pixels long along the image strip and 20 pixels wide. The afterglow was sufficiently intense to cause pile-up in the PC mode data until the third orbit. To account for this effect the source events were extracted in an annulus with a 20-pixel outer radius ($\sim 47''$) and a 3-pixel inner radius. These radii were derived by comparing the observed and nominal PSF. For the PC data collected after the third orbit, the entire circular region (20-pixel radius) was used, instead. The selected extraction regions correspond to ~ 93.5 % (WT), ~ 47.4 % (piled-up PC), and ~ 88.5 % (non piled-up PC) of the XRT PSF. These fractions were applied to correct the measurements to the full count rate. The background was measured from data within an annulus (radii 70 and 130 pixels) centered on the source (PC mode), and within a rectangular box (40×20 pixels) far from background sources (WT mode).

Spectra of the source and background were extracted in the regions described in above from the first orbit event files. Ancillary response files were generated with the task `xrtmkarf` within FTOOLS, with RMF (v007) spectral redistribution matrices. The 0.5–10 keV WT data and 0.2–10 keV PC data were simultaneously fit to an absorbed power law model, with Galactic $N_{\rm H}^{\rm Gal} = 1.75 \times 10^{21}$ cm^{-2}, and a free $N_{\rm H}$ parameter at the GRB redshift. A free constant factor was introduced to take into account the decrease of the mean flux between WT and PC data. The result is a photon index $\Gamma = 2.06 \pm 0.09$ and a column density of $N_{\rm H} = 7.91^{+4.24}_{-3.68} \times 10^{21}$ cm^{-2} (90% errors for one interesting parameter). There is no evidence for strong spectral changes after the first orbit. The GRB 051109A count rates were then converted to 0.2–10 keV unabsorbed fluxes (presented in Table 3) using the best spectral fit.

BAT data were used for γ-ray comparisons in *Swift* bursts. For these, the event files from the public archives were analyzed with the BATTOOLS and XSPEC11 software packages[4] . Using the appropriate housekeeping files, mask weighting was determined with `batmaskwtevt`, then signal-to-noise binned lightcurves were made with `batbinevt`. Spectral response (`.pha` and `.rsp`) files were created for specific time intervals using `batbinevt,`

[4]`http://swift.gsfc.nasa.gov/docs/swift/analysis/`

`batupdatephakw, batphasyserr` and `batdrmgen`. XSPEC11 fit photon indices and returned unabsorbed flux values (15–150 keV) from the `.pha` and `.rsp` files. The comparison of count rates and returned fluxes yields a general conversion factor that can be applied to transform a count rate lightcurve to fluxes.

4. Results

For these two bursts, there is a significant overlap between the early optical observations and much higher energy emission (X-ray or γ-ray). Temporal and spectral comparisons can elucidate whether the higher and lower energy emission come from the same spectral component or emitters. GRB 051109A has good temporal overlap between the optical and X-ray observations. The GRB 051111 early optical lightcurve has significant overlap with the γ-ray lightcurve, allowing a comparison of the lightcurve evolution in both bands. This section describes the conversions required for these comparisons from the photometry in Tables 1 and 2, or *Swift* data.

We determine the onset of γ-ray emission, referred to as t_{GRB}, by examining the BAT lightcurves for these events. The adopted onset for GRB 051109A is UT 01:12:15.5. This is compatible with the time of initial BAT detections reported by Fenimore et al. (2005). The adopted onset time for GRB 051111 is UT 05:59:39, congruent with the report of *Suzaku*'s initial γ-ray detection time (Yamaoka et al. 2005).

4.1. Optical Transformations to Flux Density

In the following, all comparisons from the optical to the higher frequencies use R band optical flux densities corrected for Galactic extinction unless explicitly indicated otherwise. All magnitudes from Tables 1 and 2 are converted using the effective frequencies and zero point fluxes of Bessell (1979). In particular, the R-equivalent values are converted as if they were R. This includes the ROTSE C_R and MDM r_R magnitudes. These values are corrected for extinction with the prescription of Schlegel et al. (1998). The resulting corrections are 0.511 and 0.433 mags of Galactic extinction in the R band for GRB 051109A and GRB 051111 respectively. These corrections are applied to all R-equivalent (C_R and r_R) observations.

4.2. Summary of Key Optical Features

Figure 1 gives the GRB 051109A optical lightcurve. The host flux is significant by 1 Msec. Its value, 1.4 ± 0.2 μJy, is fit from the entire lightcurve and subtracted in the figure to show the afterglow evolution.

As the dataset combines C_R and r_R data, we allow for a color offset between them, which is evident during the significant overlap from $\sim$ 2–20 ksec post-onset. The term is a simple multiplicative factor (1.5×, see Table 4) for the flux density, fitted with the optical lightcurve. It is applied to the MDM data as plotted in Figure 1. A color term of 1.5× (0.4 mag) is substantial. However, it ited r observations calibrated to R standards to unfiltered data, effectively two different optical bands near R. The MDM data during the overlap hints at a shallower evolution than the ROTSE data, but separate fits show this is not a significant result. The figure shows that with the color term, the two lightcurves are in agreement.

The first 5-second ROTSE data point for GRB 051109A is contemporaneous with γ-ray emission. The optical afterglow of GRB 051109A follows a power law decline at this time, behavior previously observed in GRB 050401 (Rykoff et al. 2005b). In this case, the early optical afterglow steepens between the early observations (until 10 ksec), and the next night. A double power law fit exhibits an initial decline of $t^{-0.652\pm0.008}$ until a time 52 ± 9 ksec, when it transitions to $t^{-1.5\pm0.2}$ (see Table 4). This describes the data adequately, as seen in Fig. 1, but has $\chi^2 = 96$ for 62 degrees of freedom (DOF). We note that the sparser data after 1 day leaves the final decay less well-constrained. Without the final observation, there would be no host constraint, and the lightcurve would appear to have a more shallow decay and an earlier optical break.

Figure 2 shows the GRB 051111 optical lightcurve. The optical is well-described by power law evolution, with breaks. There are two breaks, from an initial decay to a slightly flatter evolution at about 2 minutes post-onset, and then to a steeper decay near 0.5 hr post-onset. The latter break is discussed in § 6.4, while the former resembles an optical excess during the γ-ray emission, discussed in § 7.

Using least-squares fitting, the optical lightcurve is characterized by a triple power law (Table 4). Initially, it decays as $t^{-0.88\pm0.02}$, then at $t = 120 \pm 20$ sec, it flattens slightly to $t^{-0.74\pm0.01}$, and finally at 1100 ± 90 sec, it steepens to $t^{-1.17\pm0.02}$. This fit includes the final MDM R-band point with no color term relative to the ROTSE C_R, but the results are not affected if the fit is performed without the MDM point. The overall decay does not change between 10 and 100 ksec post-burst (although there may be some fluctuation about the power law, see Butler et al. 2006).

The existence of the initial steeper decay and the first optical break is visible to the eye

and statistically well-established. The triple power law fit gives a χ^2 of 78 for 83 DOF. A double power law can also be fit to the data, resulting in a single break at 1500 sec and a χ^2 of 98 for 85 DOF. Both fits yield acceptable χ^2, but the double power law fit has larger systematic residuals. An F-test indicates that the decrease in χ^2 by allowing the early, third power law segment is statistically significant at a confidence level greater than 0.999.

In both Figures 1 and 2, the optical decay has begun a steady decline by the first observations. These two events are well-sampled examples where the optical decay is established in a form like the fireball model afterglow during the end of the prompt emission, only tens of seconds after the start of the GRB. This is in contrast to some other cases, where the optical is rising during (GRB 050820A, Vestrand et al. 2006) or after (GRB 060605, Schaefer et al. 2006) the prompt emission.

4.3. High-Energy Data Transformations to Flux Densities

We use the GRB 051109A XRT fluxes from Table 3. These de-absorbed X-ray fluxes are converted to flux densities using the spectral fit. The spectrum's power law photon index (2.06 ± 0.09) yields a weighted mean frequency of 5.7×10^{17} Hz and a conversion factor of 4.35×10^4Jy per erg s^{-1}cm^{-2} (adding a further uncertainty of 5%) to convert to flux density.

We obtained the γ-ray data for these events from the BAT observations in the *Swift* public archive. These are reduced with the standard suite of BATTOOLS (see § 3) to produce spectral fits, count rates, and fluxes as needed.

For GRB 051109A, the BAT fluxes were analyzed by checking spectral fits over the entire burst (-10 to 50 sec post-onset), yielding $\Gamma = 1.50 \pm 0.15$. Analysis from -10 to 5 and 5 to 50 sec showed consistent photon indices, so there is no evidence for spectral evolution throughout this burst. Thus spectral parameters fitted from the entire burst were used to produce fluxes and flux densities in the BAT band from count rates. This method was also used in analyzing other events, as described in § 7.1.

For GRB 051111, the BATTOOLS spectral fits show that the BAT spectral index softens from 1.22 ± 0.04 (-5 to 10 sec) to 1.48 ± 0.07 (10 to 100 sec). The times of interest all occur during the later interval, and this interval's value of of Γ is used to convert from count rate to flux density.

BAT and XRT fluxes were also compared (for GRB 051109A) using the BAT flux spectrally extrapolated to the XRT energy range. The best determination of the BAT spectrum is obtained via XSPEC11 fits to the entire data set. The BAT fit parameters allow a flux

extrapolation in XSPEC11 from the total BAT count rate to the flux in the XRT energy band. The extrapolation can be applied to each BAT data point in the count rate light curve.

4.4. Summary of Key High Frequency Features

Figure 1 shows the GRB 051109A XRT lightcurve for this event. There is a data gap from 205 to 3400 sec, due to orbital constraints. We examined the data both by fitting before and after the gap independently, as well as fitting the entire dataset. All the results are presented in Table 4.

The first orbit data, from 134.0 to 204.5 sec post-onset, shows a steep decline as $t^{-3.2\pm0.4}$ while during this stage the optical decays at a much slower rate. The later observations, from 3.4 to 1400 ksec, show the X-ray flux declining more shallowly.

Considered in isolation, the X-ray data after the first orbit shows similar behavior to the optical lightcurve, a double power law, but with a shallower break. Initially decaying $\sim t^{-1}$, at approximately 30 ksec, it would steepen to $t^{-1.3}$. The back-extrapolation of this fit is brighter than the X-ray flux level at the end of the first orbit. This requires a near-"plateau" as the overall flux evolution throughout the data gap (an unseen fourth power law segment in the lightcurve).

The entire X-ray dataset can be fit by a triple power law: $t^{-3.3}$ shallowing to $t^{-0.6}$ at 200 sec, then steepening to $t^{-1.2}$ at 7 ksec. Due to data uncertainty, both fits, linked and unlinked across the data gap, are statistically good (χ^2 reported in Table 4). The triple power law fit is driven by the data gap: the data at 6 ksec does not show an evident break, and fitting the data before and after the gap separately yields a fit at late times that best matches ($t^{-1.32}$) just the late time behavior. The fit residuals for the model over the entire XRT dataset appear to show trends near the 6 ksec break and the late-time decay, however they are not statistically unreasonable using the "runs test" for the signs of residuals. The interpretation of the data can accomodate significant variation in the break time (30 vs. 7 ksec) and final decay ($t^{-1.3}$ vs. $t^{-1.2}$).

We note that the early XRT decay differs from the behavior through the data gap. GRB 051109A XRT observations began after the end of γ-ray emission. The prompt high-energy emission was spectrally extrapolated to the XRT band for comparison. Initally comparable in flux, the XRT decay is steeper than that implied from the flux extrapolations from the BAT during the period from $\sim$1 sec to 1 minute from the GRB onset. This would be consistent with the interpretation of steep X-ray emission from high-latitude photons, at

the end of the GRB.

Figure 3 shows the GRB 051111 BAT lightcurve. The BAT lightcurve from 15–200 sec post-onset (a time range chosen for comparison with the optical lightcurve which begins at 31.9 sec) is fit as $t^{-1.50\pm0.07}$ ($\chi^2 = 41$ for 32 DOF). The temporal behavior is fit using the count rate lightcurve, to avoid the additional uncertainty in the conversion from count rate to flux density. The count rate fit is normalized at 31.9 sec, with an amplitude that corresponds to a flux density of 81.7 ± 4.1 μJy at a weighted mean frequency of 1.7×10^{19}Hz.

5. Fireball Model Features for Interpretation

Both GRB 051111 and GRB 051109A exhibit optical lightcurve breaks at early times. To interpret these events, we use the simple fireball model (Meszaros & Rees 1997; Sari et al. 1998). This section describes the model's predicted spectral and lightcurve evolution rate characteristics that are relevant for optical and higher-energy frequencies (Piran 2005, fully reviews the model). Later sections will demonstrate that the optical and X-ray lightcurve breaks cannot be explained by the model predictions outlined below.

The fireball describes the emission from a population of accelerated electrons with Lorentz factor distribution $N(\gamma_e) \propto \gamma_e^{-p}$. The afterglow spectrum has spectral breaks: principally ν_m, due to the mimimum Lorentz factor γ_e, and ν_c, the cooling frequency. There is also a self-absorption frequency, but it is far below the optical when the optical transient flux is decaying.

The electron index p determines the synchrotron flux spectral shape. Each spectral region has a spectral index β, with flux density $f_\nu \propto \nu^\beta$. The index $\beta = (1-p)/2$ for $\nu_m < \nu < \nu_c$, and $\beta = -p/2$ for the case when $\nu > \nu_c$ and $\nu > \nu_m$. (When $\nu_c < \nu_m$, the spectral shape is $\nu^{-1/2}$ for frequencies between them.) The frequencies evolve in time depending upon geometry and the circumburst density distribution $n(r)$. The standard assumptions for the density are n constant ("ISM" case), or $n \propto r^{-2}$ ("windlike" case).

Each spectral region (relative to the break frequencies) and density regime has a relation between the lightcurve temporal evolution and p, e.g., $f_\nu \propto t^{3(1-p)/4}$ for $\nu_m < \nu < \nu_c$ in the ISM case for spherical geometry. These relations require $p > 2$. Otherwise either the total energy diverges or there is a high-energy cutoff that drives the flux evolution at a different rate.

The fireball model predicts lightcurve breaks due to both spectral evolution from the cooling adiabatic shock, and hydrodynamic transitions. While the fireball will produce rising

lightcurves at low frequencies (attenuating self-absorption, or the approach of the spectral peak), above the peak, the flux decays. The high-frequency lightcurves are expected to steepen.

Spectral evolution will produce chromatic breaks, with break frequencies evolving typically $\sim t^{-0.5}$–$t^{-1.5}$. The steepening follows a pattern, and is predicted to be shallow.

The cooling frequency, ν_c, is expected to produce a break. It evolves as $t^{-1/2}$ for an ISM density, and $t^{1/2}$ for a windlike one. With an ISM density, the cooling frequency will start high. As ν_c sweeps below a frequency, its lightcurve acquires a dependence upon ν_c and steepens by $\Delta\alpha = -0.25$, so higher frequencies will have steeper decays. A windlike density follows the opposite pattern, as ν_c sweeps *up*, making lightcurves shallower for frequencies $\nu > \nu_c$. Lightcurves of frequencies $\nu_m < \nu < \nu_c$ are steeper by $\Delta\alpha = -0.25$ than of frequencies where $\nu_m < \nu_c < \nu$.

The passage of ν_m steepens a decaying lightcurve when $\nu_c < \nu_m$. When $\nu_c < \nu < \nu_m$, the lightcurve decays shallowly (with $f_\nu \propto t^{-1/4}$) for both ISM and windlike cases. It then steepens to the decay rate above ν_c and ν_m. This requires a very shallow initial decay. The passage of ν_c is the relevant case for changes in temporal evolution of lightcurves that decay faster than $t^{-1/4}$.

Hydrodynamic changes can also provide lightcurve breaks. As the whole shock is affected, these breaks would be achromatic. The simple model predicts a "jet break" due to observing the effects of collimated ejecta. A (sharp-edged) cone of ejecta initially evolves hydrodynamically as if it were isotropic. When the ejecta have slowed sufficiently for the emission's beaming angle to be larger than the ejecta's opening angle, there will be a break due to the "missing light" compared to a spherical distribution of emitters. By geometric arguments, this would require a steepening by $\Delta\alpha = -0.75$. At approximately this time, the ejecta will begin expanding significantly sideways, putting more energy into expansion and further weakening the observed emission. The model expectation would be a larger $\Delta\alpha$, leading to a final lightcurve decay of t^{-p} (again, for $p > 2$) at all frequencies above the spectral peak.

In the simple formulation, a chromatic break would be shallow and due to ν_c, while an achromatic break would be strong and due to the jet. As discussed below, the lightcurve breaks in the GRB 051111 and GRB 051109A do not follow these predictions.

6. Evidence for Long-Term Energy Injection in Optical and X-ray

The GRB 051109A optical and X-ray lightcurves overlap for several decades in time. Although the data gaps allow some ambiguity, under any interpretation, the comparison of optical and X-ray evolution requires processes beyond the simple self-similar adiabatic fireball model.

6.1. The First Hour: X-ray and Optical Behavior Compared

§4.4 discusses the ambiguous measurements of the early X-ray lightcurve evolution. The data can be fit by the nearly-canonical triple power law shape, with the shallow segment during the orbital data gap. A fit to the data after the gap yields a later, shallower break (see Table 4).

As discussed in §5, the fireball model predicts a shallow chromatic break or a strong achomatic break. However, the two X-ray fits, when compared to the optical lightcurve, follow neither pattern.

First, if the X-ray afterglow follows the triple power law shape, there are similar strong steepenings in the X-ray and optical bands hours after the GRB, but the X-ray break occurs before the optical one. This is not characteristic of a jet or any other hydrodynamic transition.

The X-ray triple power law is suggested by the lightcurve morphology from early analysis of XRT afterglows (Nousek et al. 2006, with 27 events). However, some XRT lightcurves do not follow that pattern; in 40 cases O'Brien et al. (2006) identify several without the shallow or "hump" phase. These include examples with a single power law from early times onwards, either very steep (e.g., GRB 050421), or less so (e.g., GRB 050721). There are also cases where flares obscure where a "shallow" lightcurve segment may be (e.g., GRB 050908). If GRB 051109A's X-ray afterglow followed the steep–shallow–steep pattern, the data gap would coincidentally include the entire shallow segment. There is no information to determine whether GRB 051109A's X-ray decayed shallowly ($t^{-0.6}$) from 200 to 3400 sec, or had a more complex lightcurve evolution.

The second possible interpretation treats the data before and after the data gap (0.2–3 ksec) separately. Hours after the burst, it yields a shallow break, at the same time as the shallow optical break (thus not following the simple fireball predictions). The X-ray fit after the gap back-extrapolates to a flux brighter than observed at $t \approx 0.2$ ksec. This requires a more complex discontinuity in the X-ray evolution. The optical has well-sampled steady

decay during the X-ray's data gap, which makes the implied discontinuous X-ray evolution difficult to explain in a broadband context.

Under this interpretation, during the data gap, the X-ray lightcurve must brighten relative to its previous decay. This would be explained if the X-ray afterglow rose between orbits. However, the afterglow peak is already below the optical. The optical flux decay during the XRT data gap shows that $\nu_m < \nu_{\rm OPT} < \nu_X$, and the afterglow would already have risen at X-ray frequencies.

A flatter X-ray evolution before 3.4 ksec would be expected if ν_c dropped below the X-ray band at that time. A break passage coincident with the end of a data gap would be surprising. This interpretation is also unlikely due to the lack of evidence for change in X-ray spectrum between the first orbit and the second; the spectral index steepens by 0.5 when ν_c passes.

One possibility is an unseen flare (at XRT frequencies, during the data gap) that does not decline to the original underlying level (see rare examples in O'Brien et al. 2006, Fig. 2). Such a flare would have to have no effect upon the optical evolution, steady during this time. This would be surprising as the similar X-ray and optical decays appear to indicate a common emission source by the X-ray's second orbit. Any effect that boosts the flux level in the X-ray would be expected to have some effects in the optical. There is no physical parameter in the fireball model upon which the flux at high frequencies depends that the flux at lower frequencies (above the spectral peak) does not. Specifically, if energy is injected to raise the flux level, it will affect the entire spectrum.

By 40 sec post-onset, the optical remnant of GRB 051109A has begun a steady decline consistent with the synchrotron model from an external shock (with the steady addition of energy). The X-ray emission is not compatible with the afterglow until some time between 0.2 and 3.4 ksec. The establishment of emission from the assumed self-similar forward shock appears more complex at high energies than at low ones.

6.2. GRB 051109A: X-ray and Optical Breaks Near 0.5 Day

The optical lightcurve for GRB 051109A has a break approximately half a day after the burst. The XRT lightcurve steepens on a similar timescale.

A lack of full coverage limits our knowledge of these breaks in both bands. The optical lightcurve has sparse coverage after about 20 ksec and has a strong host contribution by 1 Msec. This prevents a precise measurement of the break time and post-break decay. The

optical steepening may be significant, but at $\Delta\alpha_{OPT} = -0.8 \pm 0.2$ it is also consistent within $3\,\sigma$ of a shallow ($\Delta\alpha = -0.25$) cooling break. The XRT data gap (200–3400 sec) prevents a good measurement of the segment before the break. The X-ray may transition from a quite shallow ($t^{-0.6}$) decay around 2 hours, with $\Delta\alpha_X = -0.64$, or it may have an initially steeper evolution (t^{-1}) with a break of $\Delta\alpha_X = -0.28$ near 9 hours. The shape of the afterglow lightcurves is more uncertain than the statistical error bars of model-fit decay rates and transition times (Table 4).

There is a transition at both frequencies at a comparable time. If the steepening were due to a break frequency passing from the X-ray to the optical, the break would have to evolve at least as fast as $\sim \nu \propto t^{-3.5}$ (if the X-ray break is around 7 ksec), or even $\sim \nu \propto t^{-17}$ (if the X-ray break is at 34 ksec). This is faster than any break evolution expected in the fireball model. With the uncertainty in break times, the optical and X-ray lightcurves are consistent with an achromatic break time. Due to the significant uncertainty in the optical steepening $\Delta\alpha$, the lightcurves are consistent with having the same amount of steepening $\Delta\alpha$.

Using the fits from Table 4, we find the spectral index from the optical to the X-ray before and after the breaks near 0.5 days. The results are $\beta_{OPT-X} = -0.65 \pm 0.15$ (-0.8 ± 0.2) at 6 (100) ksec. The consistency of β_{OPT-X} across the observed shallow breaks also points to the X-ray and optical breaks arising from a single cause, producing an achromatic effect upon the spectrum of a single emission source.

6.2.1. Fireball Spectral Constraints

The position of spectral breaks relative to the observed frequencies can be constrained via β and α. Given the uncertainties in the optical and X-ray decay rates and lightcurve breaks, more than one type of fireball model could explain the GRB 051109A afterglow data.

After the breaks at $\sim$0.5 days, the optical apparently decays more quickly than the X-ray, at $t^{-1.5\pm0.2}$. However, there is significant uncertainty in this decay rate; by refitting with various fixed decay indices α, we find the optical decay may be as shallow as $t^{-1.1}$ ($3\,\sigma$ significance). This would be consistent with the X-ray decay being steeper than the optical decay by $\Delta\alpha \approx -0.25$ before and after this break, if the X-ray was decaying as steeply as t^{-1} at $t \approx 3$ ksec, after the data gap.

As $\beta = -p/2 < -1$ when $\nu > \nu_m, \nu_c$, the relatively shallow $\beta_{OPT-X} \approx -0.7$ points to $\nu_c > \nu_{OPT}$, with ν_c above or just below the X-ray. After the 0.5 day breaks, if the X-ray is decaying as $t^{-1.3}$ and the optical as $t^{-1.1}$, ν_c would be between the optical and X-ray and the

circumburst density would be constant, like the ISM (in the windlike case, higher ν do not decay more quickly than lower ν). This would require an electron energy index $p \approx 2.4$, and point to the interpretation that the X-ray was decaying more quickly than the optical before the 0.5 day break as well. Alternatively, if both the X-ray and optical are decaying $\sim t^{-1.3}$ after the break, the shallow β_{OPT-X} would indicate $\nu_m < \nu_{OPT} < \nu_X < \nu_c$, which would be satisfied for a windlike medium with $p \approx 2.4$ and for an ISM medium with $p \approx 2.7$.

6.3. Does the Fireball Model Explain the Breaks Near 0.5 Day?

The GRB 051109A afterglow lightcurves have shapes somewhere between the two (X-ray) cases inferred from the data. The ordinary fireball model does not easily explain either the case of simultaneous optical and X-ray breaks (with a shallow $\Delta\alpha_X$) or that of both $\Delta\alpha \approx -0.7$ (with the optical break later than the X-ray).

If the breaks occur at the same time, they do not resemble the expected achromatic jet break steepening. The X-ray break appears far shallower (051109A XRT 2 in Table 4 $\Delta\alpha \approx -0.3$) than the minimum $\Delta\alpha = -0.75$ for a non-spreading jet (§5). Moreover, the pre-break decays (GRB 051109A and XRT 2 in Table 4) are not well explained by the fireball model. As the X-ray decay is apparently steeper than the optical initially, the model indicated would be an ISM density with $\nu_m < \nu_{OPT} < \nu_c < \nu_X$. Then the quite shallow optical decay is difficult to interpret, as it indicates an electron energy index $p = 1.87 \pm 0.01$, a value $p < 2$ resulting from relations that assume $p > 2$.

The alternate interpretation has an X-ray decay $\sim t^{-0.6}$ during the data gap, and the X-ray break before the optical break. The shallow early decay is still difficult to interpret. While the break amplitudes $\Delta\alpha \approx -0.7$ (both bands) could be interpreted as arising from a non-expanding jet, the break times are not achromatic as expected. Interpreting the late X-ray decay as post-jet also calls into question all afterglow interpretations. Decays of $t^{-1.3}$ have been routinely observed in afterglows on $\sim$ day timescales, and interpreted as spherical fireball behavior with typical electron energy indices $p \approx 2.4$.

Puzzling behavior has been observed in early broadband afterglow data. Some cases show chromatic early lightcurve breaks, seen only in the X-ray while the optical decay rate remains constant (Panaitescu et al. 2006). Others show simultaneous optical and X-ray breaks (e.g., GRB 050525A and GRB 050801, Blustin et al. 2006; Rykoff et al. 2006). The GRB 050801 afterglow break was achromatic for optical and X-ray frequencies, but did not have the characteristics of a jet break (Rykoff et al. 2006). The nearest analogy to GRB 051109A may be the GRB 050525A afterglow, which exhibited both optical and

X–ray steepening at $t \approx 4$ hours, with break amplitudes differing between the frequencies (Blustin et al. 2006). The final GRB 050525A lightcurve decays are quite steep (nearly $\sim t^{-2}$), and Blustin et al. (2006) tentatively conclude it is a jet break. Such a steep decay is not observed in GRB 051109A.

6.3.1. No Obvious Explanation by Complex $n(r)$

Under either lightcurve interpretation, a more complex environment cannot be easily used to produce the breaks. A change in density gradient would be a hydrodynamic change, and would produce an achromatic effect. The effect would be tiny for frequencies above both ν_c and ν_m. An achromatic break time appears to require an X-ray decay initially steeper than optical, so ν_c would be between the frequencies, and only a transition in the optical would be expected. Disregarding the break times, it is quite difficult to produce a transition from $t^{-0.65}$ to $t^{-1.2}$. If the latter is an ISM model fireball observed between ν_m and ν_c, it implies $p \approx 2.7$. Such a steep energy index would not produce a shallow $t^{-0.65}$ decay even with a sharply rising density gradient (see Yost et al. 2003, Table 5).

An alternative environmental effect such as variable extinction would have to affect frequencies from optical to the X-ray in the same fashion, which is not reasonable for known absorbers. Thus, environmental changes do not provide a plausible solution.

6.3.2. No Obvious Explanation by Changing Burst Parameters

We checked whether changing the physical parameters of the fireball could readily explain the observed lightcurves. Beyond the general question of early energy injection, recent analyses of early chromatic break cases have opened the question of changing microphysical parameters (Panaitescu et al. 2006).

As mentioned above (§ 6.3), a shallow $t^{-0.65}$ decay could imply a hard $p < 2$. A steepening of p would conceivably produce the lightcurve breaks (particularly if both bands were indeed shallow early on, with the same transition to a final decay rate). This possibility still presents a difficulty, as the spectral index would also steepen. For a sufficiently significant steepening of p, $\Delta\beta_{OPT-X} \sim -0.5$, and the ratio of X-ray to optical flux would drop by more than a factor of 10 during the transition at $t > 20$ ksec. This is not observed (Fig. 1).

It is also difficult to produce the lightcurve breaks by changing the electron or magnetic energy fractions, ϵ_e or ϵ_B. Even a shallow lightcurve break would require significant parameter changes (see the spectrum's dependences upon physical parameters, summarized

by Piran 2005). We note that generic microphysical parameter changes have many degrees of freedom, if ϵ_e, ϵ_B, and p can vary independently. As such, this is a poorly-constrained hypothesis for the various "flattened" early decays in GRB afterglows.

A more physically-motivated parameter change is the continuous injection of energy into the forward shock. Such a change would in general slow the lightcurve decay, causing a break when the injection ends. This simple formulation would not be able to explain a steepening in the X-ray before the optical, and the GRB 051109A afterglow lightcurves do not definitely have an achromatic break. However, the similar timescales for the steepening of optical and X-ray lightcurves suggest such a common cause.

Increased energy could be provided in a burst when the engine emits a distribution of material with Lorentz factors distributed in a power law ($M(\gamma) \propto \gamma^{-S}$, e.g., Sari & Mészáros 2000). The gradual "catching up" of material to the slowing forward shock increases the shock energy and decreases the flux decay rate. This model affects both spectral regions above the peak (above and below ν_c), giving them a comparable amount of flattening. This explanation can provide the appropriate level of pre-break flattening for GRB 051109A, both at optical and X-ray, with an influx of material with Lorentz factors distributed as $M(\gamma) \sim \gamma^{-4}$.

6.4. GRB 051111 Optical Break at 0.5 hours: Similarity to GRB 051109A

The optical afterglow of GRB 051111 shows a break at 1200 sec with amplitude similar to the GRB 051109A break (Table 4). Its amplitude, $\Delta\alpha = -0.43 \pm 0.03$, is too large to be due to the passage of the spectrum's cooling break. It is also too shallow to be interpreted as a jet break. There is no overlapping X-ray data for comparison, but it shares the characteristics that make the GRB 051109A afterglow break incompatible with the simple fireball model.

The decay post-break is consistent with several simple fireball scenarios. For GRB 051111 at $t > 1200$ sec, the decay can be fit by an ISM or windlike medium, with the optical above the peak and the cooling frequency of the synchrotron spectrum. The decay is also consistent with the optical above the spectral peak but below the cooling frequency, although in the windlike case the decay rate would imply a hard electron energy distribution, with $p \approx 2$.

The RUCCD data (Table 2) give rough VRI information at 1 hour post-burst. We used the data to constrain the optical spectral slope at this time. The values were corrected by 0.537, 0.433, 0.314 magnitudes for Galactic extinction in V, R, and I respectively. The data did not have the precision required to determine the spectral shape, but a fit to a power law for the three points yields a β_{OPT} of -0.4 ± 1.0. This result is consistent with all

spectral scenarios for the density regimes discussed above. It slightly favors the cases where the optical band is still below the cooling frequency at this time, which give harder optical spectra.

The decay pre-break is difficult to reconcile with the standard fireball model expectations. Using the $p > 2$ relations for this shallow decay results in an inconsistent value of $p < 2$ for a windlike medium in any spectral ordering, or for an ISM medium above the cooling frequency. The ISM medium model, with the optical between the peak and ν_c, would be just consistent with $p = 2$. As the ISM model finds p significantly above 2 post-break, it leaves the break unexplained.

6.5. Breaks From Halting Energy Injection?

The afterglow of GRB 051109A has a break observed at optical and X-ray frequencies at a similar time, tens of ksec post-burst. Data sampling gaps do not permit a definite determination of whether the break was achromatic, yet even a near proximity in time suggests a common cause. Geometric and environmental characteristics do not provide a plausible explanation, but the end of a stage of smooth energy injection could steepen lightcurves as observed.

The GRB 051111 break may be due to similar causes as the GRB051109A afterglow break. As in the GRB 051109A case, the GRB 051111 optical afterglow's shallow decay also lasts substantially longer than the prompt γ-ray detections (until 1200 sec cf. 80 sec). The GRB 051111 break can also be explained by continued energy injection from the GRB time until the break time.

7. GRB 051111: A Prompt Optical Component Consistent with the extension of the γ-rays

We now discuss the high-energy comparison for the early GRB 051111 optical observations. There is no early X-ray temporal overlap, but a significant overlap with γ-ray observations. The "90% fluence duration" of the burst is $T_{90} = 47 \pm 1$ sec in the 15–350 kev band (Krimm et al. 2005a), and the flux has a smooth decay from 10 sec after the onset that extends to 80 sec post-trigger (see Figure 3). From the onset t_{GRB} (05:59:39, see §4), three optical points are contained within T_{90}, and seven are at $t - t_{GRB} < 80$ sec. We can compare not just a single point to the γ-ray emission, but rather the optical evolution to the γ-ray evolution, as fitted from their lightcurves.

The optical lightcurve at $t < 125$ sec is brighter than the extrapolation of the ∼125–1000 sec data to earlier times. The decay before 125 sec is steeper than afterwards, which suggests an "excess component" during the GRB emission. The "excess" would be the difference between the observed emission and the extrapolation of the later, shallower emission to this early time. Taking the difference between the data and the back-extrapolation of the power law which dominates from $\approx$ 0.1–1 ksec gives an estimate of the excess component. The difference is well-fit by a power law decay of $t^{-1.8\pm0.4}$.

The implied $t^{-1.8}$ decay rate of the excess could be expected for a reverse shock component (Sari & Piran 1999), but it would be a surprising coincidence for an excess to arise from a reverse shock component lasting precisely the GRB timescale. The GRB decline is $\alpha_\gamma = -1.50\pm0.07$ (§ 4.4), so it is possible that the excess is correlated with the GRB emission (as in the case of GRB 041219A, Vestrand et al. 2005). As the GRB has a single peak with a smooth tail during the optical observations, it is not possible to establish a correlation from lightcurve morphology.

As discussed in § 4.2, the data permit a fit by a double power law with a single break at $t \sim 1$ ksec, which would imply no early excess. The triple power law from which we infer an excess is visible and statistically established by the fit improvement. Yet due to the data's uncertainties, a fit to a double power law plus an excess power law component will find an acceptable fit with no early excess component. The properties of the excess component cannot be constrained with such a general fit model.

As the above estimate of the early optical excess is consistent with the γ-ray lightcurve decay, we attempt to refine the component's estimation under the assumption that its decay is linked to the contemporaneous γ-ray lightcurve. We consider the optical flux density data for $t < 1$ ksec and the γ-ray count rates from 15–150 sec. This dataset was fit to a function $At^{\alpha_1} + Bt^{\alpha_2}$ (optical) and Ct^{α_1} (γ-rays). A Monte Carlo method determined the fit parameter uncertainties. Artificial datasets were generated, using the measured values and uncertainties to form Gaussian distributions for each data point, and then fit, yielding the distributions of the function's parameters.

With 2000 trials, $\alpha_1 = -1.44 \pm 0.07$ and $\alpha_2 = -0.70 \pm 0.03$. These are consistent with the previous measurement of this phase's γ-ray decay and α_2 in the triple power law fit (Table 4) respectively. The estimated optical excess at 31.9 sec (A) is 8.2 ± 2.1 mJy. The distribution for A is nearly Gaussian, and $A > 0$ is significant at above the 3 σ level. This estimation of the optical excess agrees with the "implied excess" from the triple power law fit at the 1.5 σ level.

We compare both the total optical flux and the estimated excess optical flux to the γ-ray

spectral extrapolation. The total optical flux density at the early time is a good match for a simple extension of the γ-ray power law spectrum. We determine $\beta_{OPT-\gamma} = -0.554 \pm 0.005$ at 31.9 sec, while $\beta_\gamma = -0.48 \pm 0.07$. These are compatible; the optical flux at this time could be produced by the low-frequency tail of the GRB. Two elements argue against this interpretation. First, it would require a sudden change from optical flux entirely due to the GRB component during the first exposure, to a similar optical flux entirely due to the afterglow seconds later. This is not a reasonable model. Secondly, the total optical decay rate is significantly shallower than the γ-ray decay as discussed above. Thus we compare the flux densities of the optical excess and the γ-rays and find the spectral index between them, $\beta = -0.44 \pm 0.03$, is also compatible with β_γ. The optical excess, considering both its temporal decay (α) and its flux level, could be produced by a spectrally unbroken low-frequency extension of the GRB. This is demonstrated in Fig. 4, which compares uncertainty contours for flux densities and α.

In conclusion, the prompt optical data of GRB 051111 has an excess over later optical evolution. The "excess" optical flux is consistent with an extra component from the GRB emission. In this case, the optical emission from the "GRB proper" is a simple extension of the GRB spectrum from the BAT band of 15–150 keV, and the spectral index from the optical excess to the γ-rays is consistent with the spectral index within the γ-ray band. This is unexpected, as there must eventually be a GRB spectral rollover at low frequencies.

7.1. Comparison of Prompt Detections

There have now been several cases with optical emission detected contemporaneously with the γ-rays: GRB 990123, GRB 041219A, GRB 050319 (see Appendix A), GRB 050401, and GRB 050904, along with GRB 051111 (discussed above) and GRB 051109A (as mentioned in § 4.1, the first ROTSE point overlaps with the tail end of GRB emission). There is no single behavior among this group, spectrally or in lightcurve evolution.

The prompt optical emission of GRB 990123 had an optical excess above later afterglow evolution that was not correlated with the GRB peaks (Akerlof et al. 1999), GRB 041219A had optical emission correlated with the GRB evolution (Vestrand et al. 2005; Blake et al. 2005), and GRB 050401 had no detectable excess prompt optical emission (Rykoff et al. 2005b). GRB 050319 is similar to GRB 050401 in that the prompt optical detection (1st point) does not deviate from the lightcurve (see Quimby et al. 2006). Boër et al. (2006) discuss optical emission during the very long, high-redshift GRB 050904. They detect optical flaring contemporaneously with X-ray flaring, at the end of γ-ray emission, but do not discuss the optical comparison to the γ-rays.

The optical-to-γ spectral indices, $\beta_{OPT-\gamma}$, and γ-ray band spectral indices, β_γ, are summarized in Table 5 and plotted in Figure 5. Appendix A describes the sources of this information. The indices are compared to see if any other events could have prompt optical emission as an unbroken spectral extension of the γ-rays. In addition to GRB 051111, the GRB 050904 event is a good candidate for such a component. There are other possible examples, but the spectral constraints are considerably poorer. GRB 051109A is compatible with a prompt optical extension, but the spectrum in the γ-rays has significant uncertainty. The first time interval considered for the broadband comparison in GRB 041219A may be compatible; the γ-ray spectral shape at the low end of the γ-ray band is poorly constrained.

GRB 050904 was a very long (in our reference frame) high-z GRB. The TAROT observations of Boër et al. (2006) have an initial upper limit, two constant detections, a flare, then upper limits. Only the first two optical observations, up to 254 sec, have significant BAT flux (the 90% flux duration is 225 ± 10 sec, Sakamoto et al. 2005a). The second observation (the first optical detection) is used to get $\beta_{OPT-\gamma}$. This spectral index is compatible with an extension of the BAT photon index (measured during the optical observation from 169 to 254 sec post-onset). However, the BAT flux fades away by the next optical observation, and the Boër et al. (2006) optical flux does not. The two components may not be from the same emission source.

Thus GRB 051111 may be unusual, with a prompt optical component compatible with the interpretation of a simple spectral extrapolation from the γ-rays. There are several cases of prompt optical observations, and no dominant behavior in the relative optical/γ comparisons.

Beyond the extrapolation of β_γ to the optical, the comparison of $\beta_{OPT-\gamma}$ and β_γ are not always compatible with a single prompt synchrotron spectrum. In the case of GRB 990123, the prompt optical flux is well above the γ-ray spectral extrapolation and $\beta_{OPT-\gamma}$ is much softer than β_γ. Connecting them requires a "valley" not seen in the synchrotron spectrum. This may also be the case for GRB 051109A, although the uncertainties in the indices are too great to make this determination. In contrast, the GRB 041219A, GRB 050319, and GRB 050401 optical flux is well below the γ-ray spectral extrapolation. These cases would be compatible with a synchrotron spectrum having its flux density peak between the optical and γ-ray frequencies. GRB 041219A (with an optical/γ lightcurve correlation, Vestrand et al. 2005) would imply a prompt $p \approx 2$–2.7 for $\beta_\gamma = (1-p)/2$ (or $-p/2$ for the last time interval tabled). For the cases of GRB 050319 and GRB 050401, there is no lightcurve correlation and $\beta_{OPT-\gamma}$ with β_γ would imply a synchrotron peak at ≈ 0.5, 3 keV, respectively.

7.2. Implications

The GRB 051109A and GRB 051111 events continue to confirm what has been previously noted in prompt comparisons: that there can often be a prompt optical afterglow component distinct from the low-energy emission tail of the GRB. In both cases, the prompt optical emission smoothly connects to the later afterglow (albeit with an excess component for GRB 051111). In the context of the fireball model, this would appear to indicate that the deceleration and thus the establishment of the external shock occurs earlier than the end of high-energy emission. A separate afterglow component distinct from the prompt emission is also implied by the likely interpretation of Nousek et al. (2006)'s standard XRT afterglow shape. The initial fast decline may be high-latitude emission from the end of the prompt GRB emission component, superimposed on the shallower, distinct afterglow component.

The existence of separate prompt and afterglow components is relevant to the question of GRB emission models. The "external–external" shock model (Meszaros & Rees 1993) posits that the GRB's γ-ray emission is produced by the fireball's external shock, and not by other means, such as internal shocks within the relativistic flow. GRB variability would be due to interactions with a clumpy external medium. This model has been proposed as an explanation for GRBs with a small number of γ-ray lightcurve peaks, such as GRB 991216 (Ruffini et al. 2002), and GRB 970508 (one of 10 GRBs with simple lightcurves analyzed by McMahon et al. 2004). McMahon et al. (2004) examined the afterglow fits and extrapolated the results to fluxes at the prompt GRB band. With a single external shock, the afterglow would connect directly to the GRB. Despite GRB 051111's simple BAT lightcurve (see Fig. 3), it does not fit the external–external picture. It has two components during the GRB – a prompt optical excess and the already-established afterglow. Its optical decay changes after the end of GRB emission and does not extend from the "excess" component apparently connected to the γ-ray emission.

8. Conclusions

GRB 051109A and GRB 051111 are two of the best-sampled cases to analyze broadband comparisons of the prompt and very early post-burst optical lightcurves to higher energy emission. The results continue to show that there are diverse processes occurring during the early afterglow phase.

GRB 051109A has a break in both the optical and the X-ray near 0.5 day post-burst. It is consistent with being an achromatic transition, although the X-ray data sampling does not permit this to be firmly established. The breaks are shallower than expected for a jet

break, and are most easily explained by the cessation of steady energy injection into the afterglow forward shock. The initial establishment of the afterglow may be more complex at high energies (X-ray) than at low ones (optical).

GRB 051111's optical lightcurve decays more steeply during the prompt emission than after the end of γ-ray detection. This indicates a prompt excess above the continuing afterglow emission. Given the temporal coincidence of the excess with the GRB emission, and its flux level compatible with a spectral extrapolation of the γ-ray flux, we interpret the excess as emission connected to the GRB. We do not consider a reverse shock interpretation as likely. A separate component for prompt emission, disconnected with the ongoing afterglow emission, is not compatible with the external–external shock model for this single-peaked γ-ray event.

In comparison to other prompt detections, the GRB 051111 optical component is unusual. The GRB 051109A event may show optical flux at a level compatible with a direct extrapolation of the γ-ray flux, but it is not as well constrained. In the GRB 041219A event, with an optical lightcurve correlated with the GRB emission (Vestrand et al. 2005), the flux level cannot be simply extrapolated. A spectral break is implied between the optical and γ-ray frequencies.

In both GRB 051109A and GRB 051111, the afterglow emission is ongoing during the prompt γ-ray emission. In these cases the deceleration time to establish the external shock expected to power the afterglow is shorter than the GRB duration. This is in contrast to other cases where the afterglow is rising throughout or after the prompt emission (GRB 050820A, GRB060605, Vestrand et al. 2006; Schaefer et al. 2006, respectively). There are a variety of apparent afterglow rise times, thus models of the GRB event and progenitor environment must be capable to explaining such diverse results.

At tens of seconds after the GRB onset, the emitters are ultrarelativistic and near the progenitor environment ($\sim$ light-week). GRB studies continue to uncover evidence of a wide variety of processes underlying the emission during this early phase. There is optical emission of the "afterglow" type during the burst in both cases presented here. With present capabilities it may only be rarely possible to observe the "afterglow onset" (rise of the forward shock) if it is usually well-established during the GRB itself. The dearth of reverse shock signatures and evidence of steady energy input for up to hours post-burst are clues to dynamic processes at the heart of the collapse of massive stars. We are learning that simple calculations are insufficient to address such data. It is difficult to disentangle all source and environmental effects in order to study the ultrarelativistic emission. The most promising avenue of study uses prompt and early simultaneous observations at widely separated frequencies. This coverage shows evidence that in some events, such as GRB 051109A, different

frequencies resolve themselves to the steady afterglow flux declines over different timescales. Such observations may shed light on the early emission.

ROTSE-III has been supported by NASA grant NNG-04WC41G, NSF grant AST-0407061, the Australian Research Council, the University of New South Wales, the University of Texas, and the University of Michigan. Work performed at LANL is supported through internal LDRD funding. Special thanks to the observatory staff at McDonald Observatory, especially David Doss.

XRT work is supported at Observatorio Astronomica di Brera and INAF-IASF Palermo by ASI grant I/R/039/04

The MDM work has been supported by the National Science Foundation under grant 0206051 to JPH.

The US Air Force provided the telescope time for RUCCD observations, as well as on-site support and 80% of the research funds for the AFOSR and NSF jointly sponsored research, under grant number NSF AST-0123487. The smooth installation and operation of the RUCCD has been made possible through the extensive efforts and cooperation of the staff at the telescope, and we would like to thank everyone who has spent time helping us. Particular thanks for their help with our project go to John Africano, Spence Ah You, Paul Bellaire, Peter Figgis, John Flam, Tom Goggia, Nancy Ichikawa, Paul Kervin, Kevin Moore, Thomas Nakagawa, Karl Rehder, Lewis Roberts, David Talent, and Darius Vunck.

The Digitized Sky Surveys were produced at the Space Telescope Science Institute under U.S. Government grant NAG W-2166. The images of these surveys are based on photographic data obtained using the Oschin Schmidt Telescope on Palomar Mountain and the UK Schmidt Telescope. The plates were processed into the present compressed digital form with the permission of these institutions.

A. Data for Other Prompt Detections

In order to compare the GRB 051111 prompt optical detection with other cases, the spectral information for each event must be extracted in a consistent fashion. Thus to derive Table 5, for each event we revisit the determination of the spectral index within the γ-ray band, as well as between the optical and γ-rays.

The table gives the available simultaneous optical and γ-ray detections for bursts to date. The comparisons are based on spectral flux density, so both optical magnitudes and

γ-ray fluxes are converted to flux density at a particular frequency. The table highlights whether the optical flux is above or below the spectrum extrapolated from the γ-ray band by comparing $\beta_{OPT-\gamma}$ to β_γ. As such, the γ-ray frequency and spectral shape (β_γ) are for the *lowest* well-measured γ-ray energy. In most cases, it is simply the weighted average frequency across the energy band, given the γ-ray spectral index. When possible, the optical to γ-ray comparisons are made for more than one time interval during the prompt overlap.

The following are details concerning each burst individually.

For GRB 990123, the data are from Akerlof et al. (1999), Table 1 and Briggs et al. (1999), Table 2. The optical-to-γ ratios of Briggs et al. (1999) are adjusted to correspond to the final optical values of Akerlof et al. (1999) (corrected for 0.05 mags of extinction), rather than the GCN preliminary values. These subsequently are used to produce $\beta_{OPT-\gamma}$. No uncertainties were provided for the γ-ray flux densities, so Table 5 reports 3 significant figures, as in the source paper. The value of β_γ is taken from the Band model fits of Briggs et al. (1999) for the entire event.

For GRB 041219A, the data are from Vestrand et al. (2005) (using its Fig. 4), which corrects the optical flux for 4.9 mags of extinction. The γ-ray frequency used, ν_γ, is for the lowest energy of the four γ-ray bins. β_γ is fit for each time interval using the four γ-ray frequencies and flux densities. The first time interval has a γ-ray spectrum that is not well-fit by a single spectral index ($\chi^2 = 13$ for 2 degrees of freedom). It has two entries in Table 5. The first entry (Table 5, line 4) uses the overall least-squares fit β_γ for this time interval, despite the poor fit. The second entry (Table 5, line 5) uses β_γ from the two lowest-energy γ-ray frequency bins, which has a high uncertainty. The fourth time interval (Table 5, line 8) has only upper limits for the flux densities in the optical and the highest-energy γ ray frequency bin. The spectral index β_γ is fit from only the first 3 frequency bins.

The GRB 050319 optical point is from Quimby et al. (2006), corrected for 0.03 mags of extinction (Schlegel et al. 1998). The γ-ray data are from the *Swift* archive, analyzed with BATTOOLS to produce a flux density and β_γ. This burst had more than one peak of emission, and the soft γ-ray spectral index quoted is derived from the final peak, from 130–170 sec post-onset. The optical observations were taken after the end of the initially reported γ-ray duration (Krimm et al. 2005b). However, high-energy emission was still detected in the count rate lightcurve. The faint emission did not have high signal to noise during the 5-sec optical observation. The γ-ray flux at the optical detection time was estimated by interpolating a power law from the nearest 3 count rate data points. The result was consistent with the power law interpolation of the nearest 4 γ-ray detections in the tail of the γ-ray peak, as well as with linear interpolations using these 3 or 4 points. The signal-to-noise on the γ-ray count rate detection is approximately 7; the low apparent signal-to-noise

of the flux density reported is due to uncertainty in the count rate conversion to flux density.

The GRB 050401 data is from Rykoff et al. (2005b). The photon index is converted to β_γ. The optical flux density from Rykoff et al. (2005b), Table 1 is corrected for 0.174 mags of extinction as per Schlegel et al. (1998) at the coordinates given in the paper. The γ-ray flux density uses the complete 15–350 keV band, converting to a flux density at 140 keV using β_γ.

The GRB 050904 optical data is from Boër et al. (2006), corrected for 0.117 mags of extinction (at the OT coordinates, as per Schlegel et al. 1998) and converted to mJy. γ-ray data was taken from the *Swift* archive for this event. We used the standard BATTOOLS presciption to determine F_ν and β_γ. We separated the data into two response files (during and post-slew for this interval), and combined them in XSPEC. As there is sufficient signal for a good spectral extraction over the optical overlap t_{start}–t_{end}, β_γ is from this time interval only. The asymmetric error bars are a result of this extraction. The uncertainty in $\beta_{OPT-\gamma}$ compares the maximum optical and minimum γ-ray (and vice-versa) to calculate the range of β. The optical overlap analyzed here is the second interval (T2) of the Boër et al. (2006) observations. However, the first interval had only an optical limit. The third interval had a similar optical flux to T2, but the γ-ray flux is almost undetectable, as the GRB T_{90} duration is 225 ± 10 sec (Sakamoto et al. 2005a). Therefore other optical comparisons were not well constrained. The evolution of this event is further discussed in § 7.1.

The GRB 051109A optical data is taken from Table 1, with an extinction correction of 0.511 mags (see § 4.1). The γ-ray data are from the *Swift* archive, analyzed with BATTOOLS to produce a flux density and β_γ. The spectral index β_γ is for the entire burst duration; there is no evidence of spectral evolution when the γ-ray data is divided into two time bins. The symmetric $F_\nu(\nu_\gamma)$ error bars are statistical; the asymmetric ones are the additional uncertainty in the conversion of count rate to flux. Similarly, the index $\beta_{OPT-\gamma}$ has asymmetric error bars from the count rate conversion uncertainty in the γ-ray flux density.

For GRB 051111, the optical data is from Table 1, de-extincted by 0.433 mags (see § 4.1). The γ-ray data are from the *Swift* archive, as detailed in § 3. In brief, standard BATTOOLS and XSPEC11 analysis were employed to extract spectral information for the event as a whole, as well as the early (-5 to 10 sec) and late (10 to 50 sec) parts of the burst (roughly divided to halve the signal). The burst softened from early to late; the photon index of the late part of the burst was used to produce the comparison β_γ. The optical and γ-ray flux densities are compared in two different ways at the midpoint of the first optical point (31.9 sec). The γ-ray flux density is derived from a fit to the BAT lightcurve for $t > 15$ sec, which is well-fit by a power law $t^{-1.50\pm0.07}$. The first optical flux comparison is to the initial optical detection. The second is to the "excess" optical flux above the later,

shallower optical decay after the end of the GRB. While it is nominally at 31.9 sec, the optical excess is derived from the lightcurve evolution. Line 13 uses the actual optical observation from Table 1, de-extincted. Line 14 uses the estimated "optical excess" from § 7 to make the $\beta_{OPT-\gamma}$ comparison.

REFERENCES

Akerlof, C., et al. 1999, Nature, 398, 400

Akerlof, C. W., et al. Jan. 2003, PASP, 115, 132

Bertin, E. & Arnouts, S. June 1996, A&AS, 117, 393

Bessell, M. S. Oct. 1979, PASP, 91, 589

Blake, C. H., et al. May 2005, Nature, 435, 181

Blustin, A. J., et al. Feb. 2006, ApJ, 637, 901

Boër, M., Atteia, J. L., Damerdji, Y., Gendre, B., Klotz, A., & Stratta, G. Feb. 2006, ApJ, 638, L71

Briggs, M. S., et al. Oct. 1999, ApJ, 524, 82

Burrows, D. N., et al. Oct. 2005, Space Science Reviews, 120, 165

Butler, N. R., et al. June 2006, astro-ph/0606763

Christensen, L., Hjorth, J., & Gorosabel, J. Oct. 2004, A&A, 425, 913

Fenimore, E., et al. 2005, GCN Circ. No. 4217

Gehrels, N., et al. Aug. 2004, ApJ, 611, 1005

Hill, G., Prochaska, J. X., Fox, D., Schaefer, B., & Reed, M. 2005, GCN Circ. No. 4255

Kennicutt, R. C. 1998, ARA&A, 36, 189

Krimm, H., et al. 2005, GCN Circ. No. 4260

Krimm, H., et al. 2005, GCN Circ. No. 3117

Liang, E. P., Crider, A., Böttcher, M., & Smith, I. A. July 1999, ApJ, 519, L21

McMahon, E., Kumar, P., & Panaitescu, A. Nov. 2004, MNRAS, 354, 915

Meszaros, P. & Rees, M. J. Mar. 1993, ApJ, 405, 278

Meszaros, P. & Rees, M. J. Feb. 1997, ApJ, 476, 232

Meszaros, P., Rees, M. J., & Papathanassiou, H. Sept. 1994, ApJ, 432, 181

Moretti, A., et al. Mar. 2006, A&A, 448, L9

Nousek, J. A., et al. May 2006, ApJ, 642, 389

O'Brien, P. T., et al. Aug. 2006, ApJ, 647, 1213

Panaitescu, A., Mészáros, P., Burrows, D., Nousek, J., Gehrels, N., O'Brien, P., & Willingale, R. July 2006, MNRAS, 369, 2059

Piran, T. 2005, Reviews of Modern Physics, 76, 1143

Quimby, R., Fox, D., Hoeflich, P., Roman, B., & Wheeler, J. C. 2005, GCN Circ. No. 4221

Quimby, R. M., et al. Mar. 2006, ApJ, 640, 402

Ruffini, R., Bianco, C. L., Chardonnet, P., Fraschetti, F., & Xue, S.-S. Dec. 2002, ApJ, 581, L19

Rujopakarn, W., Swan, H., Rykoff, E. S., & Schaefer, B. 2005, GCN Circ. No. 4247

Rykoff, E. S., et al. Feb. 2006, ApJ, 638, L5

Rykoff, E. S., Schaefer, B., Rujopakarn, W., Yuan, F., & Quimby, R. 2005, GCN Circ. No. 4211

Rykoff, E. S., et al. Oct. 2005, ApJ, 631, L121

Sakamoto, T., et al. 2005, GCN Circ. No. 3938

Sakamoto, T., Burrows, D., Immler, S., Gehrels, N., Hunsberger, S., Marshall, F., Palmer, D., & La Parola, V. 2005, GCN Circ. No. 4248

Sari, R. & Mészáros, P. May 2000, ApJ, 535, L33

Sari, R. & Piran, T. Aug. 1999, ApJ, 520, 641

Sari, R., Piran, T., & Narayan, R. Apr, 1998, ApJ, 497, L17

Schaefer, B. E., Rykoff, E. S., Smith, D. A., & Quimby, R. 2006, GCN Circ. No. 5222

Schlegel, D. J., Finkbeiner, D. P., & Davis, M. June 1998, ApJ, 500, 525

Smith, I. A., Dufour, R. J., Liang, E. P., Silverman, J. M., Hardin, L. C., Forgey, R. D., Skinner, M. A., Alday, A., & Ah You, S. 2005, , in AMOS Technical Conference Proceedings, Wailea, Maui, HI, 2005 September 5-9

Smith, I. A. & Swan, H. F. 2005, GCN Circ. No. 4267

Stetson, P. B. Mar. 1987, PASP, 99, 191

Tagliaferri, G., et al. 2005, GCN Circ. No. 4213

Thompson, C. Oct. 1994, MNRAS, 270, 480

Usov, V. V. Apr, 1994, MNRAS, 267, 1035

Vestrand, W. T., et al. May 2005, Nature, 435, 178

Vestrand, W. T., et al. July 2006, Nature, 442, 172

Yamaoka, K., et al. 2005, GCN Circ. No. 4299

Yost, S. A., Harrison, F. A., Sari, R., & Frail, D. A. Nov. 2003, ApJ, 597, 459

This preprint was prepared with the AAS LaTeX macros v5.2.

Table 1. Optical Photometry for GRB 051109A

Telescope	Filter	$t_{\rm start}$ (s)	$t_{\rm end}$ (s)	Magnitude
ROTSE	C_R	37.2	42.2	14.991 ± 0.061
ROTSE	C_R	44.3	49.3	14.998 ± 0.062
ROTSE	C_R	51.4	56.4	15.150 ± 0.071
ROTSE	C_R	58.5	63.5	15.200 ± 0.070
ROTSE	C_R	65.6	70.6	15.347 ± 0.080
ROTSE	C_R	72.7	77.7	15.306 ± 0.079
ROTSE	C_R	79.8	84.8	15.443 ± 0.089
ROTSE	C_R	86.9	91.9	15.478 ± 0.091
ROTSE	C_R	94.1	99.1	15.368 ± 0.077
ROTSE	C_R	101.2	106.2	15.530 ± 0.092
ROTSE	C_R	119.5	139.5	15.703 ± 0.053
ROTSE	C_R	156.6	176.6	15.899 ± 0.062
ROTSE	C_R	186.2	206.2	15.960 ± 0.067
ROTSE	C_R	215.1	235.1	15.916 ± 0.059
ROTSE	C_R	245.4	265.4	16.081 ± 0.069
ROTSE	C_R	274.7	294.7	16.208 ± 0.079
ROTSE	C_R	303.8	323.8	16.199 ± 0.073
ROTSE	C_R	332.8	352.8	16.476 ± 0.096
ROTSE	C_R	361.9	381.9	16.55 ± 0.11
ROTSE	C_R	391.5	411.5	16.502 ± 0.098
ROTSE	C_R	421.0	481.0	16.468 ± 0.057
ROTSE	C_R	490.2	550.2	16.753 ± 0.070
ROTSE	C_R	559.3	619.3	16.805 ± 0.073
ROTSE	C_R	628.5	688.5	16.987 ± 0.094
ROTSE	C_R	697.6	757.6	16.912 ± 0.083
ROTSE	C_R	766.6	826.6	17.06 ± 0.10
ROTSE	C_R	835.7	895.7	17.064 ± 0.097
ROTSE	C_R	904.9	964.9	17.37 ± 0.14
ROTSE	C_R	974.0	1034	17.59 ± 0.16
ROTSE	C_R	1043	1103	17.19 ± 0.11
ROTSE	C_R	1113	1450	17.411 ± 0.069
ROTSE	C_R	1459	1796	17.559 ± 0.080
ROTSE	C_R	1805	2142	17.863 ± 0.095
ROTSE	C_R	2151	3179	17.889 ± 0.078
ROTSE	C_R	3188	4368	18.29 ± 0.14
ROTSE	C_R	4378	5406	18.19 ± 0.11
ROTSE	C_R	5415	7480	18.31 ± 0.11
ROTSE	C_R	7490	9558	18.46 ± 0.12
ROTSE	C_R	9567	12048	18.57 ± 0.13
ROTSE	C_R	12060	14540	18.90 ± 0.17
MDM	r_R	2135	2255	18.186 ± 0.048
MDM	r_R	2292	2412	18.214 ± 0.075
MDM	r_R	2448	2568	18.333 ± 0.060
MDM	r_R	2996	3296	18.365 ± 0.061
MDM	r_R	3332	3632	18.546 ± 0.067
MDM	r_R	3669	3969	18.535 ± 0.066

Table 1—Continued

Telescope	Filter	$t_{\rm start}$ (s)	$t_{\rm end}$ (s)	Magnitude
MDM	r_R	4005	4305	18.486 ± 0.081
MDM	r_R	4342	4642	18.574 ± 0.037
MDM	r_R	4678	4978	18.747 ± 0.051
MDM	r_R	5014	5314	18.835 ± 0.057
MDM	r_R	5351	5651	18.858 ± 0.071
MDM	r_R	5687	5987	18.865 ± 0.040
MDM	r_R	6023	6323	18.931 ± 0.041
MDM	r_R	6360	6660	18.933 ± 0.067
MDM	r_R	6696	6996	18.874 ± 0.074
MDM	r_R	7032	7332	18.995 ± 0.094
MDM	r_R	7368	7668	19.160 ± 0.086
MDM	r_R	7704	8004	19.022 ± 0.086
MDM	r_R	8377	8677	19.093 ± 0.066
MDM	r_R	8713	9013	19.192 ± 0.080
MDM	r_R	9049	9349	19.31 ± 0.11
MDM	r_R	10240	10840	19.159 ± 0.093
MDM	r_R	10880	12750	19.27 ± 0.17
MDM	r_R	89850	90450	21.190 ± 0.083
MDM	r_R	100600	101200	21.44 ± 0.10
MDM	r_R	264300	266100	22.48 ± 0.11
MDM	R	1.046×10^6	1.049×10^6	23.79 ± 0.17
MDM	R	2.017×10^7	2.017×10^7	23.70 ± 0.16

Note. — All times are in seconds since the burst onset, 01:12:15.5 UT (see § 2). ROTSE C_R magnitudes are for unfiltered CCD magnitudes referenced to R with the USNOB 1.0 standards. MDM r_R magnitudes are r-band observations that are referenced to R using two USNOB 1.0 R standards.

Table 2. Optical Photometry for GRB 051111

Instrument	Filter	$t_{\rm start}$ (s)	$t_{\rm end}$ (s)	Magnitude
ROTSE	C_R	29.4	34.4	13.062 ± 0.029
ROTSE	C_R	36.5	41.5	13.262 ± 0.029
ROTSE	C_R	43.6	48.6	13.372 ± 0.028
ROTSE	C_R	50.7	55.7	13.512 ± 0.032
ROTSE	C_R	57.8	62.8	13.610 ± 0.033
ROTSE	C_R	64.9	69.9	13.753 ± 0.037
ROTSE	C_R	72.0	77.0	13.798 ± 0.038
ROTSE	C_R	79.1	84.1	13.908 ± 0.039
ROTSE	C_R	86.3	91.3	14.049 ± 0.042
ROTSE	C_R	93.4	98.4	14.068 ± 0.036
ROTSE	C_R	111.4	131.4	14.352 ± 0.028
ROTSE	C_R	148.9	168.9	14.547 ± 0.031
ROTSE	C_R	177.8	197.8	14.683 ± 0.027
ROTSE	C_R	207.0	227.0	14.751 ± 0.034
ROTSE	C_R	236.8	256.8	14.885 ± 0.057
ROTSE	C_R	265.8	285.8	14.986 ± 0.049
ROTSE	C_R	295.3	315.3	14.993 ± 0.047
ROTSE	C_R	324.9	344.9	15.097 ± 0.045
ROTSE	C_R	353.9	373.9	15.156 ± 0.075
ROTSE	C_R	383.5	403.5	15.211 ± 0.049
ROTSE	C_R	412.9	432.9	15.181 ± 0.063
ROTSE	C_R	441.9	461.9	15.271 ± 0.075
ROTSE	C_R	471.0	491.0	15.346 ± 0.084
ROTSE	C_R	500.3	520.3	15.591 ± 0.099
ROTSE	C_R	529.3	549.3	15.601 ± 0.075
ROTSE	C_R	558.2	578.2	15.641 ± 0.085
ROTSE	C_R	587.8	607.8	15.487 ± 0.060
ROTSE	C_R	616.8	636.8	15.577 ± 0.050
ROTSE	C_R	645.8	665.8	15.707 ± 0.072
ROTSE	C_R	674.9	694.9	15.825 ± 0.070
ROTSE	C_R	703.9	723.9	15.844 ± 0.079
ROTSE	C_R	733.1	753.1	15.78 ± 0.11
ROTSE	C_R	762.6	782.6	15.82 ± 0.11
ROTSE	C_R	791.7	811.7	15.934 ± 0.088
ROTSE	C_R	821.2	841.2	15.897 ± 0.085
ROTSE	C_R	850.4	870.4	15.829 ± 0.078
ROTSE	C_R	879.9	899.9	15.922 ± 0.068
ROTSE	C_R	909.5	929.5	15.90 ± 0.15
ROTSE	C_R	938.4	958.4	16.03 ± 0.13
ROTSE	C_R	967.8	987.8	16.059 ± 0.089
ROTSE	C_R	996.9	1016.9	16.13 ± 0.13
ROTSE	C_R	1026	1046	16.01 ± 0.12
ROTSE	C_R	1055	1075	16.12 ± 0.10
ROTSE	C_R	1084	1104	16.08 ± 0.11
ROTSE	C_R	1114	1134	16.143 ± 0.099
ROTSE	C_R	1143	1163	16.22 ± 0.11

Table 2—Continued

Instrument	Filter	$t_{\rm start}$ (s)	$t_{\rm end}$ (s)	Magnitude
ROTSE	C_R	1173	1193	16.30 ± 0.11
ROTSE	C_R	1202	1222	16.15 ± 0.13
ROTSE	C_R	1231	1251	16.31 ± 0.12
ROTSE	C_R	1261	1281	16.25 ± 0.11
ROTSE	C_R	1290	1310	16.29 ± 0.13
ROTSE	C_R	1319	1339	16.34 ± 0.14
ROTSE	C_R	1348	1368	16.33 ± 0.12
ROTSE	C_R	1378	1398	16.39 ± 0.14
ROTSE	C_R	1407	1427	16.42 ± 0.14
ROTSE	C_R	1436	1456	16.46 ± 0.14
ROTSE	C_R	1466	1486	16.78 ± 0.21
ROTSE	C_R	1495	1515	16.46 ± 0.17
ROTSE	C_R	1524	1544	16.226 ± 0.089
ROTSE	C_R	1554	1574	16.56 ± 0.16
ROTSE	C_R	1583	1603	16.86 ± 0.19
ROTSE	C_R	1613	1633	16.66 ± 0.24
ROTSE	C_R	1642	1662	16.61 ± 0.15
ROTSE	C_R	1671	1691	16.66 ± 0.26
ROTSE	C_R	1700	1720	16.80 ± 0.20
ROTSE	C_R	1729	1749	16.68 ± 0.19
ROTSE	C_R	1758	1778	16.68 ± 0.16
ROTSE	C_R	1788	1808	16.76 ± 0.18
ROTSE	C_R	1817	1837	> 17.1
ROTSE	C_R	1846	1866	16.90 ± 0.16
ROTSE	C_R	1953	1973	16.68 ± 0.20
ROTSE	C_R	1983	2003	16.72 ± 0.27
ROTSE	C_R	2012	2032	16.87 ± 0.23
ROTSE	C_R	2042	2062	16.60 ± 0.11
ROTSE	C_R	2071	2091	16.64 ± 0.17
ROTSE	C_R	2100	2237	16.816 ± 0.084
ROTSE	C_R	2246	2383	17.04 ± 0.16
ROTSE	C_R	2392	2529	17.05 ± 0.11
ROTSE	C_R	2538	2675	17.22 ± 0.10
ROTSE	C_R	2684	2821	17.34 ± 0.15
ROTSE	C_R	2830	2968	17.315 ± 0.096
ROTSE	C_R	2977	3407	17.30 ± 0.11
ROTSE	C_R	3417	3845	17.69 ± 0.21
ROTSE	C_R	3855	4283	17.74 ± 0.16
ROTSE	C_R	4293	4721	17.86 ± 0.19
ROTSE	C_R	4730	5730	18.24 ± 0.12
ROTSE	C_R	5739	6604	18.43 ± 0.24
ROTSE	C_R	6613	8561	18.96 ± 0.37
RUCCD	V	2972[a]	4104	17.1 ± 0.3
RUCCD	R	1908[b]	2520	16.7 ± 0.4
RUCCD	R	2972[c]	4104	17.5 ± 0.2
RUCCD	I	1908[d]	2520	15.7 ± 0.3

Table 2—Continued

Instrument	Filter	$t_{\rm start}$ (s)	$t_{\rm end}$ (s)	Magnitude
RUCCD	I	2972[e]	4104	16.9 ± 0.2
MDM	R	87900	91400	21.63 ± 0.10

[a]RUCCD observations were taken by shifting through the VRI filters during this interval. The mean time of the coadded images used for this point is 3488 sec.

[b]RUCCD observations were taken by shifting through the RI filters during this interval. The mean time of the coadded images used for this point is 2350 sec.

[c]RUCCD observations were taken by shifting through the VRI filters during this interval. The mean time of the coadded images used for this point is 3794 sec.

[d]RUCCD observations were taken by shifting through the RI filters during this interval. The mean time of the coadded images used for this point is 2199 sec.

[e]RUCCD observations were taken by shifting through the VRI filters during this interval. The mean time of the coadded images used for this point is 4006 sec.

Note. — All times are in seconds since the burst onset, 05:59:39 UT (see § 2). ROTSE C_R magnitudes are for unfiltered CCD magnitudes referenced to R with the USNOB 1.0 standards.

Table 3. XRT Fluxes for GRB 051109A

$t_{\rm start}$ (ksec)	$t_{\rm end}$ (ksec)	0.2–10 keV Flux (10^{-12}erg cm^{-2}s^{-1})
0.1325	0.1355	1380±190
0.1355	0.1385	1550±210
0.1385	0.1415	1280±190
0.1415	0.1445	810±150
0.1445	0.1475	950±170
0.1475	0.1505	920±160
0.1505	0.1535	950±160
0.1535	0.1565	570±130
0.1565	0.1595	710±140
0.1595	0.1625	810±150
0.1625	0.1685	770±100
0.1685	0.1745	638±95
0.1745	0.1805	543±90
0.1805	0.1865	434±81
0.1865	0.1925	475±85
0.1925	0.1985	461±79
0.1985	0.2045	240±120
3.432	3.492	100±19
3.492	3.552	59±18
3.552	3.612	69±17
3.565	3.685	93±16
3.612	3.672	142±33
3.685	3.805	84±11
3.805	3.925	74±11
3.925	4.045	78±11
4.045	4.165	63.7±9.8
4.165	4.285	66.8±9.7
4.285	4.405	68±10
4.405	4.525	86±11
4.525	4.645	59.4±9.7
4.645	4.765	68.3±9.7
4.765	4.885	52.0±8.6
4.885	5.005	59.7±9.5
5.005	5.125	53.0±9.0
5.125	5.245	47.6±8.6
5.245	5.365	60.9±9.7
5.365	5.485	51.4±9.1
5.485	5.605	60.9±9.7
5.605	5.845	51.2±6.1
5.845	6.085	53.8±8.7
9.205	9.445	46.0±6.1
9.445	9.685	24.3±4.4
9.685	9.925	28.9±4.9
9.925	10.165	29.6±4.9

Table 3—Continued

$t_{\rm start}$ (ksec)	$t_{\rm end}$ (ksec)	0.2–10 keV Flux (10^{-12}erg cm^{-2}s^{-1})
10.17	10.41	25.9±4.4
10.41	10.65	26.5±4.5
10.65	10.89	24.8±4.7
10.89	11.13	29.4±4.6
11.13	11.37	33.9±5.0
11.37	11.61	24.8±4.7
11.61	11.85	26.1±5.7
14.92	15.31	16.6±2.8
15.31	15.70	17.7±2.1
15.70	16.09	16.9±2.0
16.09	16.48	15.4±2.0
16.48	16.87	16.6±2.1
16.87	17.26	14.0±1.9
17.26	17.65	11.4±2.0
20.77	21.16	10.3±2.0
21.16	21.55	14.7±1.9
21.55	21.94	13.5±1.9
21.94	22.33	11.3±1.8
22.33	22.72	12.5±1.8
22.72	23.11	14.7±1.9
23.11	23.50	14.5±2.5
26.62	27.01	10.6±2.7
50.59	63.08	4.14±0.30
78.67	84.90	3.40±0.38
84.94	167.08	1.290±0.099
172.6	254.6	0.65±0.12
258.8	283.5	0.472±0.076
350.7	376.1	0.382±0.076
437.5	461.7	0.239±0.059
605.1	665.3	0.163±0.030
687.4	855.3	0.161±0.027
860.0	1202	0.084±0.012
1207	1550	0.074±0.011

Note. — All times are in seconds since the burst onset, 01:12:15.5 UT (see § 2).

Table 4. Power Law Fits

Dataset	$t_0(s)$	$F_0(\mu\mathrm{Jy})$[a]	α_1	$t_{\mathrm{break}}1$(ksec)	S[b]	α_2	$t_{\mathrm{break}}2$(ksec)	S[b]	α_3	color term[c]
051109A optical[d]	na	50.6 ± 6.5	-0.6520 ± 0.0082	52.4 ± 9.2	50	-1.47 ± 0.18	na	na	na	1.513 ± 0.043
051109A XRT 1[e]	150	40.0 ± 1.8	-3.20 ± 0.36	na	na	na	na	na	na	na
051109A XRT 2[e]	na	0.35 ± 0.12	-1.036 ± 0.034	34 ± 10	9	-1.32 ± 0.032	na	na	na	na
051109A XRT[e]	na	18.7 ± 3.9	-3.28 ± 0.49	0.189 ± 0.016	-9	-0.599 ± 0.053	6.59 ± 0.62	9	-1.237 ± 0.017	na
051111 optical	na	8500 ± 1000	-0.876 ± 0.021	0.124 ± 0.018	-50	-0.742 ± 0.013	1.100 ± 0.088	50	-1.169 ± 0.022	na

[a]The normalization of a single power law is $F_0(t/t_0)^{\alpha}$, and t_0 is selected for convenience within the data's time range. The double and triple power law fits have a different normalization. The formula for a double power law is $F_0(t/t_{\mathrm{break}}1)^{\alpha_1}(1+(t/t_{\mathrm{break}}1)^{S(\alpha_1-\alpha_2)})^{-1/S}$. The formula for a triple power law is $F_0(t/t_{break\ 1})^{\alpha_1}(1+(t/t_{\mathrm{break}}1)^{S_1(\alpha_1-\alpha_2)})^{-1/S_1}(1+(t/t_{\mathrm{break}}2)^{S_2(\alpha_2-\alpha_3)})^{-1/S_2}$.

[b]The S values are sharpness parameters for the breaks (see note above). In no case was S well-determined in the fit, and fixed values are selected to produce sharp breaks.

[c]Multiplicative factor applied to MDM R-equivalent data in a fit, relative to the unfiltered R-equivalent ROTSE flux densities.

[d]The GRB 051109A optical fit is to all points including the last (host) one. A constant is added to the double power law fit model. The fitted host level is 1.40 ± 0.21 μJy, within 2.5σ of the measured host flux (corrected for extinction and the MDM color term). The MDM color term fit is dominated by the data during the MDM/ROTSE overlap, the r_R observations. A fit in which only r_R data get a color term (the last 2 MDM points left with no color term) does not affect the results.

[e]The XRT observations are divided into the first orbit (XRT 1) and all subsequent data (XRT 2). As seen in Fig. 1, there is a data gap and the early and late evolution do not match. Thus there are three fits, the first orbit (XRT 1), the later orbits (XRT 2), and an overall fit of all the data (XRT)

Note. — Data for GRB 051109A and GRB 051111 optical taken from Tables 1 and 2, corrected for Galactic extinction, and converted to flux densities as discussed in § 4.1. GRB 051109A XRT data from Table 3. Not every fit uses all the parameters tabled; when a parameter was not applicable, this is indicated in the table as "na". The values of χ^2 and degrees of freedom (DOF) for each fit are as follows: GRB 051109A optical - 96 for 62 DOF, GRB 051109A XRT 1 - 14 for 15 DOF, GRB 051109A XRT 2 - 53 for 55 DOF, GRB 051109A XRT - 70 for 71 DOF, and GRB 051111 optical - 78 for 83 DOF.

Table 5. Gamma/Optical Comparisions

GRB	$t_{start}(s)$	$t_{end}(s)$	Band	$F_\nu(\nu_{OPT})$(mJy)	$\nu_\gamma(10^{18}\mathrm{Hz})$	$F_\nu(\nu_\gamma)$ (μJy)	$\beta_\gamma = 1-\Gamma$	$\beta_{OPT-\gamma}$
990123	22.2	27.2	C_V	79.6 ± 5.1	24	4450	0.40 ± 0.01	-0.270
..	47.4	52.4	..	1090 ± 20	24	1630	..	-0.609
..	72.7	77.7	..	392 ± 11	24	1710	..	-0.508
041219A	202.9	275.5	C_R	2.88 ± 0.87	5.0 ± 1.3	738 ± 39	-0.39	-0.147 ± 0.033
041219A	..	..	..	..	..	..	-0.15 ± 0.15	-0.147 ± 0.033
..	288.0	318.0	..	10.3 ± 1.0	..	3600 ± 190	-0.508 ± 0.032	-0.113 ± 0.012
..	330.4	402.9	..	3.84 ± 0.76	..	2882 ± 75	-0.737 ± 0.024	-0.031 ± 0.021
..	415.4	573.1	..	< 1.0	..	583 ± 31	-1.344 ± 0.090	> -0.065
050319	162.8	167.8	..	1.30 ± 0.17	13	29^{+18}_{-12}	-1.21 ± 0.14	-0.372 ± 0.062
050401	33.2	38.2	..	0.69 ± 0.19	34	877 ± 28	-0.58 ± 0.06	0.026 ± 0.030
050904	169.0	253.8	C_I	$19.4^{+5.4}_{-4.0}$	18	$134.1^{+4.8}_{-12.1}$	-0.293 ± 0.063	$-0.454^{+0.024}_{-0.031}$
051109A	37.7	42.7	C_R	4.97 ± 0.28	17	$6.10^{+0.12}_{-1.71} \pm 1.47$	-0.50 ± 0.15	$-0.638^{+0.002}_{-0.031} \pm 0.024$
051111	29.4	34.4	..	27.34 ± 0.74	17	81.7 ± 4.1	-0.475 ± 0.065	-0.5539 ± 0.0054
..	31.9	31.9	..	8.1 ± 2.1	..	..	-0.475 ± 0.065	-0.438 ± 0.025

Note. — All times are in seconds since the burst onset time: UT 09:46:56.1 (GRB 990123), 01:42:18.7 (GRB 041219A), 09:29:01.4 (GRB 050319), 14:20:06 (GRB 050401), 01:51:44 (GRB 050904), 01:12:15.5 (GRB 051109A), and 05:59:39 (GRB 051111). The last two events are detailed in § 4. Appendix A gives data references and analysis, explaining individual lines event-by-event, with data references. The energy band for the BAT is 15–150 keV, and a typical γ-ray detection energy for a *Swift* event is ∼100 keV. However, lower energy γ-ray fluxes are used when a good measurement is available in order to compare the low-energy γ-ray extension. When a γ-ray flux density is reported with uncertainties larger than 1/3 of the flux value, the detection of high-energy emission in the *count rate* is greater than $3\,\sigma$ significant. The time ranges for determining the GRB photon index Γ typically extend over the entire burst time to get a good measurement, but can be for subintervals as indicated in the Appendix. The optical bands are "clear" (no filter) tied to a filter band, V, R, I as indicated in the subscript. Particularly, the Appendix explains the two lines used for GRB 041219A's first time interval (with two estimates of β_γ, and the two lines used for GRB 051111 (with two optical flux estimates).

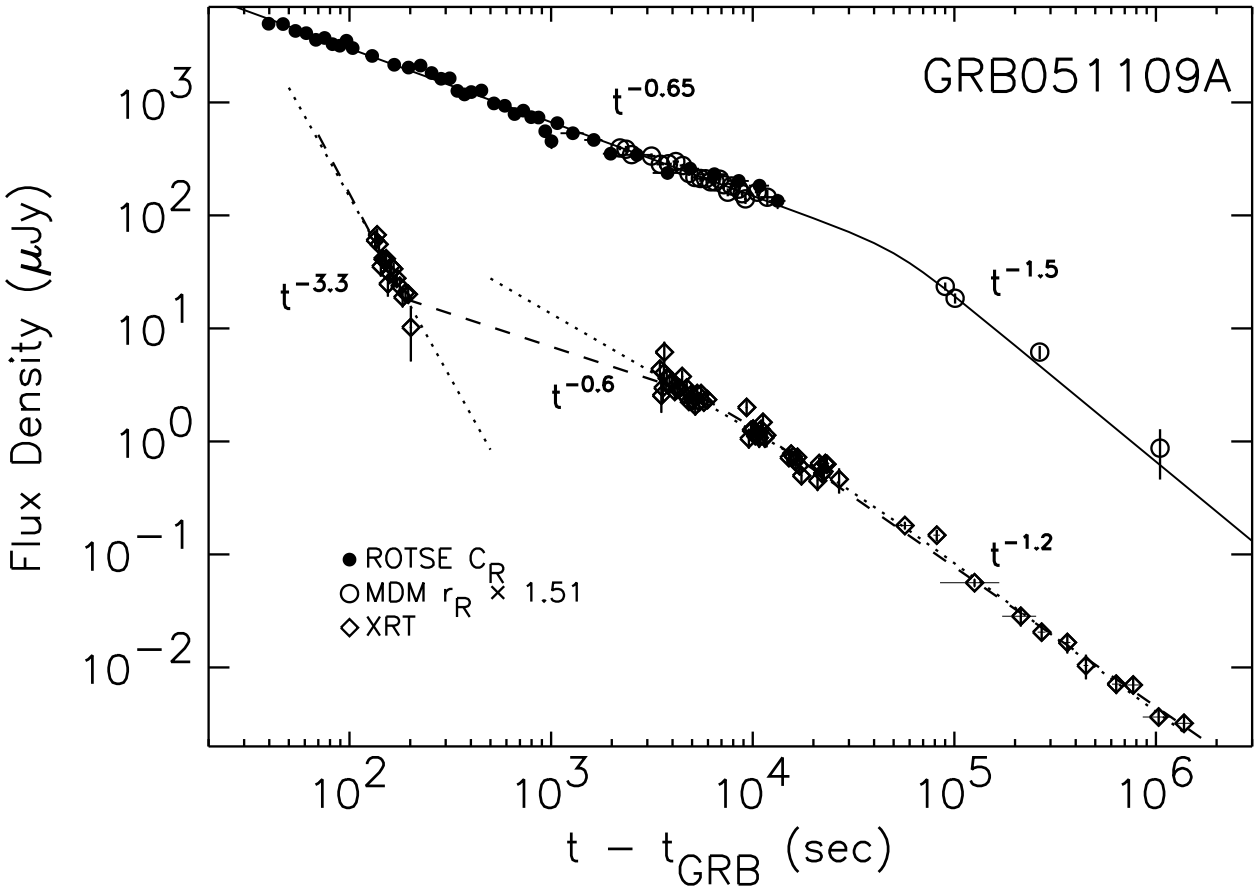

Fig. 1.— GRB 051109A optical and X-ray early lightcurves. The ROTSE magnitudes and MDM of Table 1 are converted to flux densities (and corrected for by 0.511 mag of Galactic extinction, see § 4.1), and the XRT flux density conversions are described in § 4.3. The adopted onset time t_{GRB} is UT 01:12:15.5. The optical lightcurve is fit by a double power law (see Table 4) from $t^{-0.65}$ to $t^{-1.5}$ with a break time of 50 ± 10 ksec, plus a constant host term. The fit includes a color term between the MDM R-equivalent r and the ROTSE R-equivalent unfiltered values, thus the MDM points are multiplied by the fitted factor of 1.51 on the plot. The fitted host value of 1.4 ± 0.2 μJy is subtracted from the optical lightcurve (and the final point is not plotted), in order to show the evolution of the optical afterglow light. The first XRT orbit shows a steep decay discontinuous with subsequent X-ray evolution. The later XRT data can be fit by a double power law (dotted lines showing the unlinked fits of data before and after the orbital gap), or by a triple power law (dashed line, where the shallow segment of $t^{-0.6}$ has no data to anchor it). The latter approach shows the average flux evolution through the data gap. The X-ray and the optical data, taken together, show an steepening consistent with achromaticity around 0.5 days (see § 6.2). Post-break, the decays and spectral index can be explained by an ISM or windlike model with the cooling break above the X-ray (§ 6.2.1). Pre-break, the temporal decays are too shallow to be easily explained by the fireball model, although long-duration smooth energy injection is a possibility, see § 6.3.

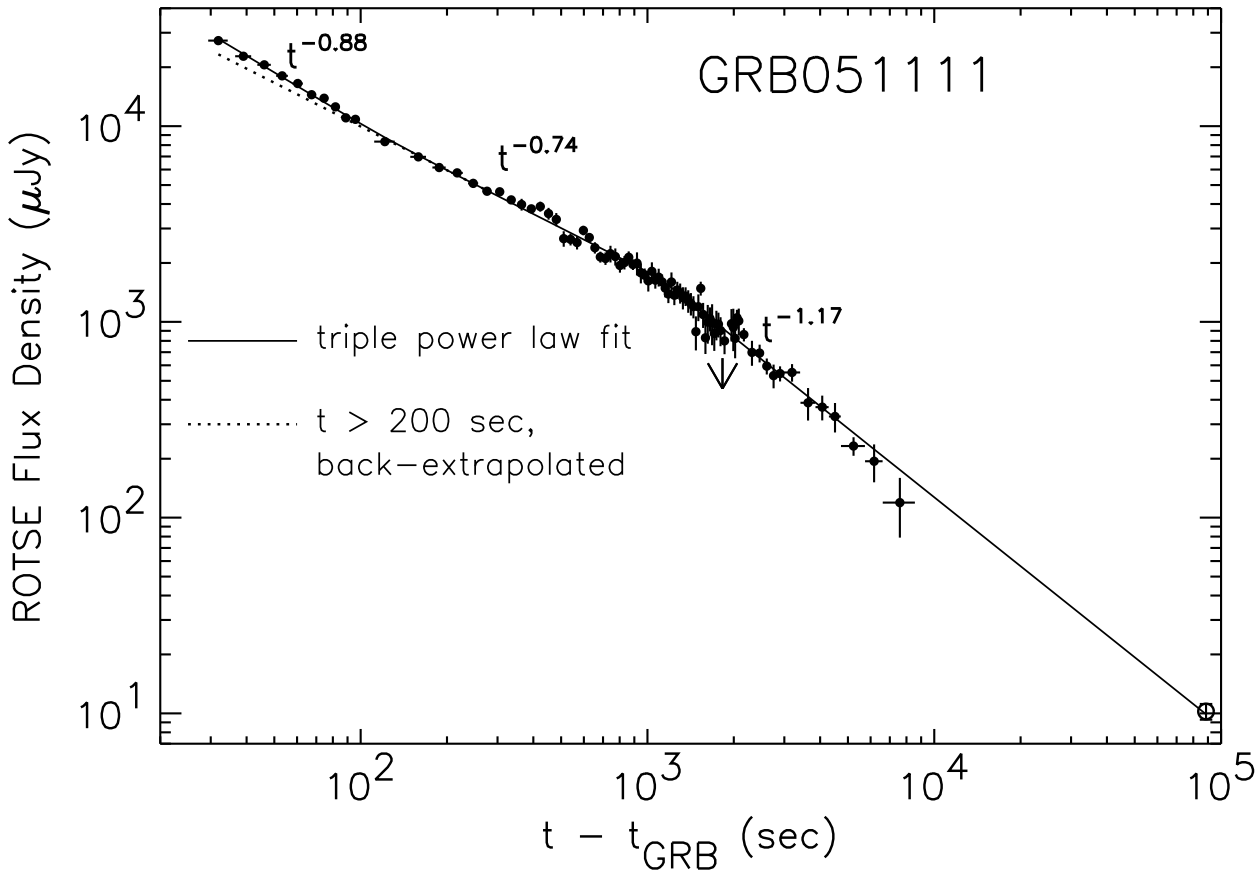

Fig. 2.— GRB 051111 optical ROTSE lightcurve. The ROTSE magnitudes of Table 2 are converted to flux densities (corrected for 0.433 mag of Galactic extinction, see § 4.1). A ROTSE observation not detected at $> 3\sigma$ significance is given as a 3σ upper limit and indicated by the arrow. A single late MDM observation is included as an unfilled point, with no color offset applied. The adopted onset time t_{GRB} is UT 05:59:39. The optical is fit with a triple power law, as described in § 4.1 and reported in Table 4 (solid line). The optical decay from 100 to 1000 sec post-onset is $t^{-0.74\pm0.01}$. The break after 1000 sec is by $\Delta\alpha = -0.43 \pm 0.03$, which does not fit any expected spectral or jet break in the simple fireball model. It may indicate a similar process as that which produces the shallow break in GRB 051109A (Fig. 1), see § 6.4. During the prompt γ-ray emission, lasting until ∼80–100 sec post-onset (see Fig. 3), the optical light decays more rapidly than after its end. The *dashed* line shows the back-extrapolation of the lightcurve's fitted power law evolution after $\sim$ 150 sec.

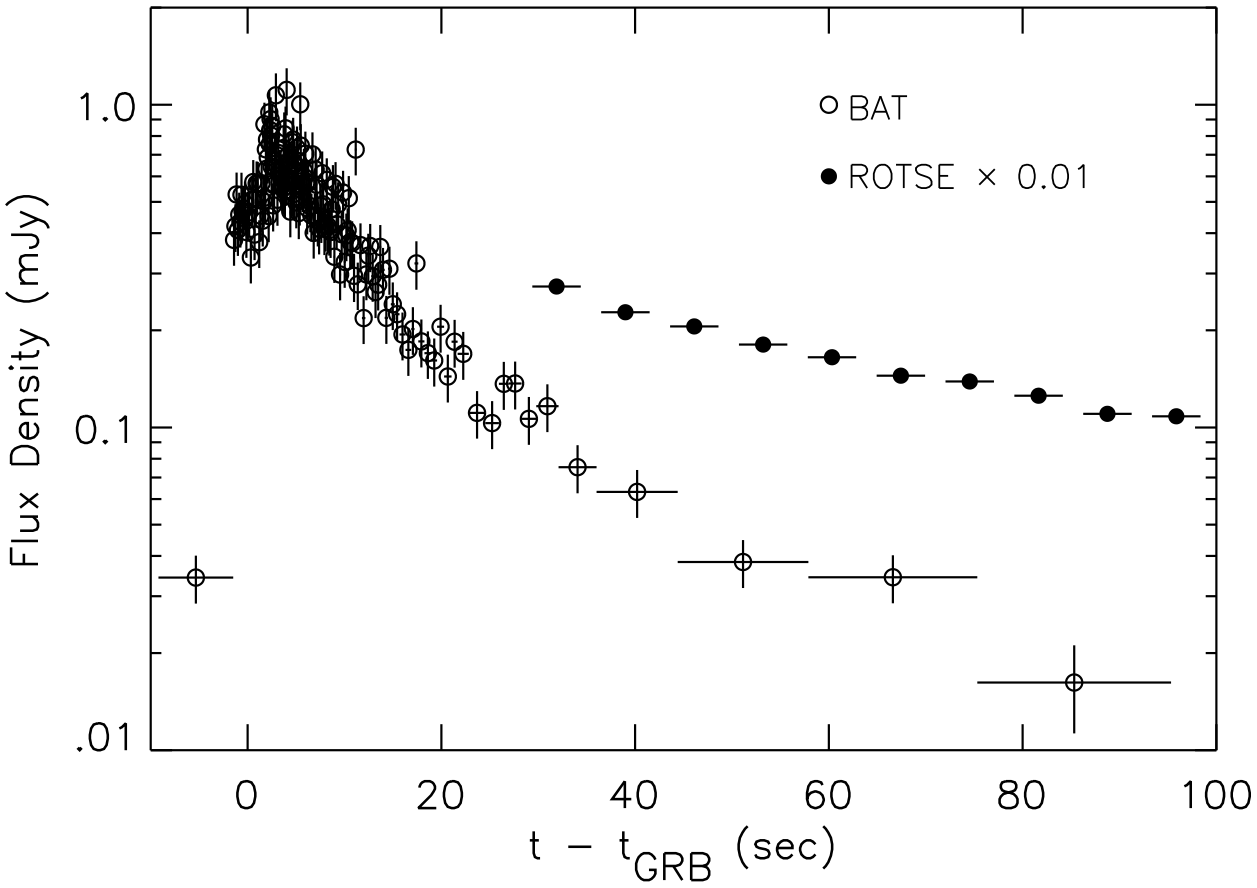

Fig. 3.— GRB 051111 *Swift* BAT 15–150 keV γ-ray lightcurve, compared to ROTSE-III prompt optical detections. The ROTSE flux densities are as described in Fig. 2, now scaled by a factor of 0.01 for comparison, and the BAT flux density conversions are described in § 4.3. The adopted onset time t_{GRB} is UT 05:59:39. The linear timescale allows the point before t_{GRB} to be shown, and thus that the onset matches the beginning of γ-ray emission. There is γ-ray emission to approximately 80–100 sec post-onset. The prompt optical flux declines more slowly than the smooth tail of γ-ray emission.

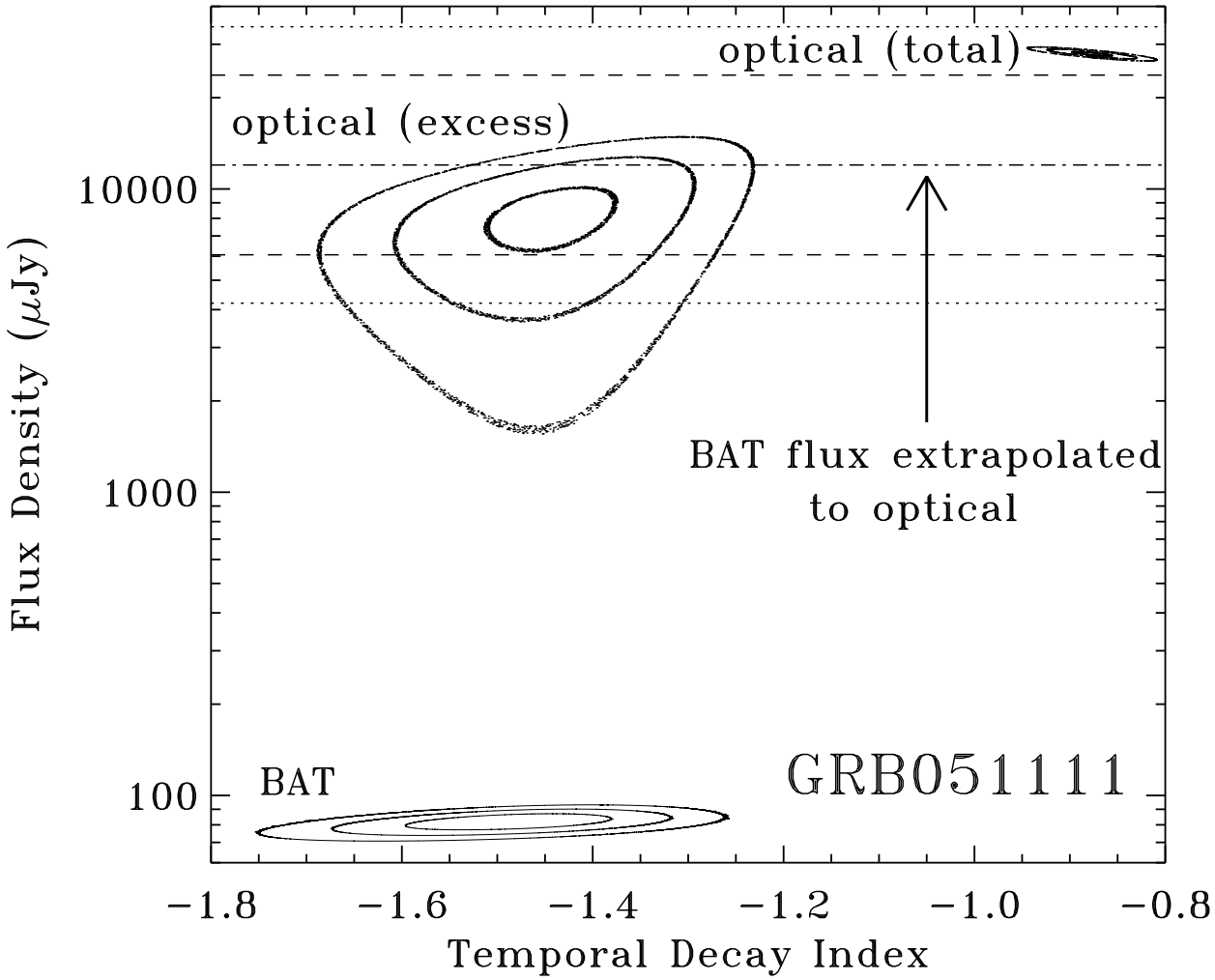

Fig. 4.— Comparing GRB 051111's prompt optical and γ-ray flux density and lightcurve evolution. Flux density is at the start of ROTSE observations, 31.9 sec after the γ-ray onset. The lightcurve evolution is measured as a power law index, α, for $f_\nu \propto t^\alpha$. The total optical lightcurve is fit from 31.9–150 sec and the γ-ray BAT lightcurve is fit from 15–200 sec. The optical excess is implied by the triple power law, with a shallow prompt phase (Table 4 and Fig. 2). The excess' implied α matches the γ-ray lightcurve. The excess is estimated by fitting the optical ($t < 1$ ksec) and γ-ray (15–200 sec) simultaneously, with an optical "afterglow" power law plus an excess constrained to have the same α as the BAT data (see §7). This optical excess fits the data well, showing a good match to the γ-ray α determined from the BAT data alone. The total optical lightcurve's index α is not a good match. The excess' flux density level is consistent with an unbroken spectral extrapolation of the BAT flux. The dot-dashed line shows the best estimate of the BAT flux density at 31.9 sec, extrapolated to optical frequencies via the photon index, Γ, (fit at $t > 10$ sec, §4.4). The dashed lines give the extrapolation range for 68% confidence limits on Γ, and dotted lines the 90% range. The prompt γ-ray emission is compatible with an unbroken extension to optical frequencies, producing the early "excess" optical component. See § 7.1 for a comparison with other cases of prompt optical emission and their optical-to-γ spectra.

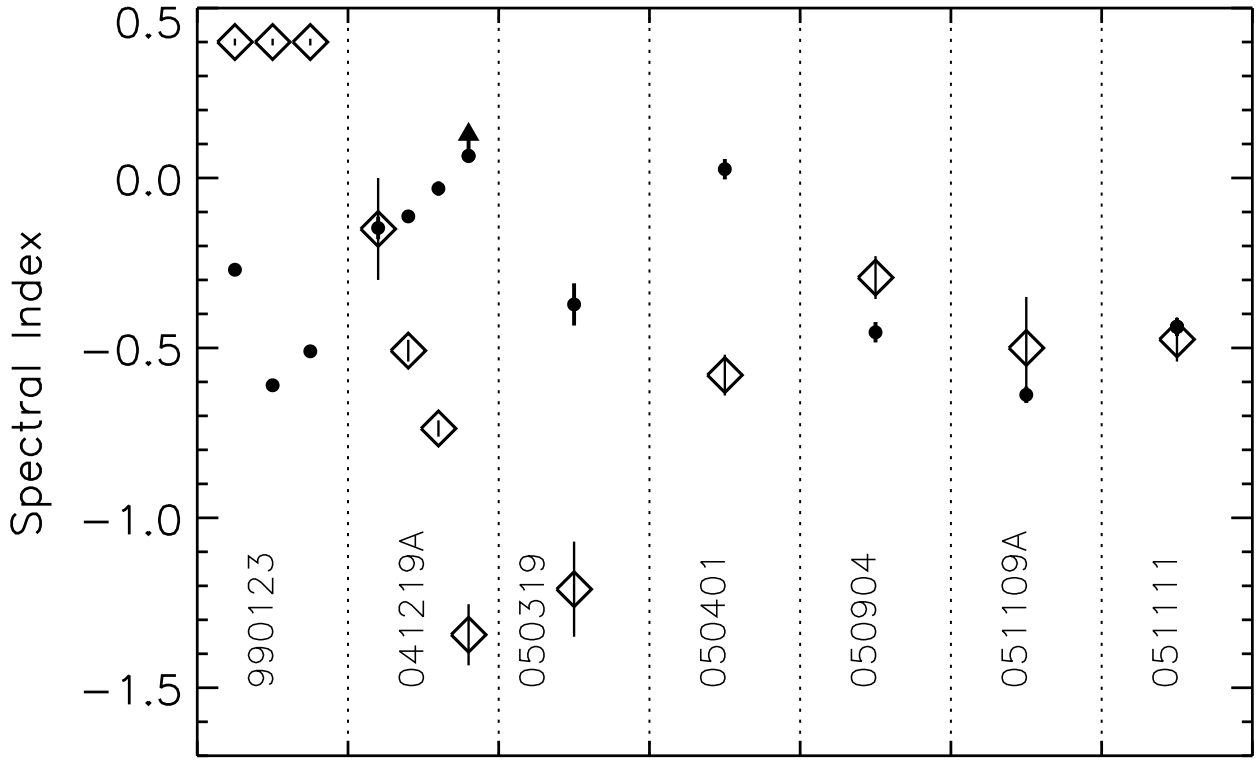

Fig. 5.— Comparison of prompt optical-to-γ-ray spectral indices ($\beta_{OPT-\gamma}$) to the spectral index within the γ-ray band (β_γ). The values in Table 5 are plotted for each event, with small solid circles for $\beta_{OPT-\gamma}$, and large open diamonds for β_γ. Multiple measurements are for events with prompt optical and γ-ray measurements during more than one time interval. The sample shows all possible orderings of $\beta_{OPT-\gamma}$ relative to β_γ. The GRB 051111 $\beta_{OPT-\gamma}$ value uses the prompt optical "excess" component, not the total optical flux. This component is consistent with an unbroken spectral extrapolation from the high-energy GRB emission, see § 7. GRB 051109A and GRB 050904 are poorer candidates for such an extension, as discussed in § 7.1. Although Vestrand et al. (2005) show a correlation in the optical and γ-ray lightcurves for GRB 041219A, there must be a spectral break, such as a synchrotron peak, between the two frequency bands.